

INFRARED AND HARD X-RAY DIAGNOSTICS OF AGN IDENTIFICATION FROM THE SWIFT/BAT AND AKARI ALL-SKY SURVEYS

K. MATSUTA^{1,2}, P. GANDHI², T. DOTANI^{2,1}, T. NAKAGAWA², N. ISOBE², Y. UEDA³, K. ICHIKAWA³,
Y. TERASHIMA⁴, S. OYABU⁵, I. YAMAMURA^{2,1}, AND L. STAWARZ^{2,6}

¹Department of Space and Astronautical Science, The Graduate University for Advanced Studies, 3-1-1 Yoshinodai, Chuo-ku, Sagamihara, Kanagawa 252-5210, Japan

²Institute of Space and Astronautical Science, Japan Aerospace Exploration Agency, 3-1-1 Yoshinodai, Chuo-ku, Sagamihara, Kanagawa 252-5210, Japan

³Department of Astronomy, Kyoto University, Kitashirakawa-Oiwake-cho, Sakyo-ku, Kyoto 606-8502, Japan

⁴Department of Physics, Ehime University, 2-5, Bunkyo-cho, Matsuyama, Ehime 790-8577, Japan

⁵Graduate School of Science, Nagoya University, Furo-cho, Chikusa-ku, Nagoya, Aichi 464-8601, Japan

⁶Astronomical Observatory, Jagiellonian University, ul. Orla 171, Kraków 30-244, Poland

Draft version October 20, 2018

ABSTRACT

We combine data from two all-sky surveys in order to study the connection between the infrared and hard X-ray (> 10 keV) properties for local active galactic nuclei (AGN). The *Swift*/Burst Alert Telescope all-sky survey provides an unbiased, flux-limited selection of hard X-ray detected AGN. Cross-correlating the 22-month hard X-ray survey with the *AKARI* all-sky survey, we studied 158 AGN detected by the *AKARI* instruments. We find a strong correlation for most AGN between the infrared (9, 18, and 90 μm) and hard X-ray (14–195 keV) luminosities, and quantify the correlation for various subsamples of AGN. Partial correlation analysis confirms the intrinsic correlation after removing the redshift contribution. The correlation for radio galaxies has a slope and normalization identical to that for Seyfert 1s, implying similar hard X-ray/infrared emission processes in both. In contrast, Compton-thick sources show a large deficit in the hard X-ray band, because high gas column densities diminish even their hard X-ray luminosities. We propose two photometric diagnostics for source classification: one is an X-ray luminosity vs. infrared color diagram, in which type 1 radio-loud AGN are well isolated from the others in the sample. The other uses the X-ray vs. infrared color as a useful redshift-independent indicator for identifying Compton-thick AGN. Importantly, Compton-thick AGN and starburst galaxies in composite systems can also be differentiated in this plane based upon their hard X-ray fluxes and dust temperatures. This diagram may be useful as a new indicator to classify objects in new and upcoming surveys such as *WISE* and *NuSTAR*.

Subject headings: galaxies: active — infrared: galaxies — X-ray: galaxies

1. INTRODUCTION

Active galactic nuclei (AGN) emit broadband emission over the entire electromagnetic spectrum. Their typical spectral energy distributions (SEDs) display a strong infrared (IR) bump around 1–100 μm , where a significant portion of their power emerges (e.g., Antonucci 1993; Elitzur 2008). Its source is considered to be a pc-scale torus of dust and gas clouds, which is heated by radiation from the nucleus and reprocesses this power into the IR, at least for the majority of AGN which are not dominated by beamed emission from relativistic jets (e.g., Elitzur 2008). The nuclear X-ray emission from AGN is produced by Comptonization of the disk emission in a hot corona above an accretion disk (Sunyaev & Titarchuk 1980; Haardt & Maraschi 1993; Zezas et al. 1998), again with a possible exception of jet-dominated sources.

It has been shown that there is a good linear correlation between the logarithms of the observed continuum emission in the mid-IR and the intrinsic soft X-ray (< 10 keV) band luminosities of local AGN, which appears to be largely independent of the amount of dust reddening (e.g., Krabbe et al. 2001; Lutz et al. 2004; Horst et al. 2006, 2008; Gandhi et al. 2009; Levenson et al. 2009; Asmus et al. 2011). This

is not expected according to pioneering AGN dust torus models (Pier & Krolik 1993), which assumed homogeneous and smooth dust distributions, because IR emission from the warm-inner clouds is expected to be dramatically scattered and reduced when viewed from an edge-on orientation. On the contrary, observations show a tight correlation with little scatter and no IR depletion, largely independent of orientation (which ought to correlate approximately with dust reddening) at all AGN luminosities. Under the torus paradigm, the correlation may be consistent with models having a clumpy obscuring geometry (e.g., Krolik & Begelman 1988; Dullemond & Dominik 2005; Hönig et al. 2006; Nenkova et al. 2008; Schartmann et al. 2008; Hönig et al. 2010; Hönig & Kishimoto 2010), in which the inner torus regions can be visible even at edge-on orientations.

However, previous works are based on small and incomplete samples, with selection criteria biased towards bright sources visible in the mid-IR from the ground, or sources in which the intrinsic soft X-ray power could be determined. Below 10 keV, AGN spectra can require detailed modeling due to the presence of several components including the underlying AGN power law, obscuration, scattering, non-thermal emission of relativistic jets (in case of radio-loud sources), and eventually thermal

emission of hot gaseous interstellar medium. Good quality X-ray spectroscopy is necessary to disentangle these. The intrinsic X-ray fluxes of Compton-thick (CT) AGN ($N_{\text{H}} > 10^{24} \text{ cm}^{-2}$), especially, are fully absorbed in soft X-ray band energies.

In this paper, our aim is to explore the X-ray vs. IR correlation using unbiased samples, and then define new and simple photometric diagnostics for AGN classification. We use the *Swift*/Burst Alert Telescope (BAT) hard X-ray ($> 10 \text{ keV}$) survey as the base AGN selection catalog. The hard X-ray energy band is rather insensitive to the intervening column density up to mildly CT columns. The survey reflects the intrinsic luminosity of the source and provides samples largely unbiased by obscuration. We use the *Swift*/BAT 22-month Source Catalog herein (Tueller et al. 2010). Several recent works explored the connection of hard X-rays with near-IR powers and with mid-IR emission line properties (e.g., Mushotzky et al. 2008; Diamond-Stanic et al. 2009; Rigby et al. 2009; Weaver et al. 2010), but correlation with an all-sky mid-IR survey at high angular resolution is still lacking.

High angular resolution is crucial in order to properly separate AGN from stellar emission in the IR (e.g., Gandhi et al. 2009; Horst et al. 2009; Vasudevan et al. 2010; Mullaney et al. 2011). For many years, *IRAS* provided the most complete all-sky survey (Joint *IRAS* Science 1994), but with an angular resolution only of order arcmins. The *AKARI* satellite (Murakami et al. 2007) has now completed its all-sky survey which is several times more sensitive than *IRAS*, and at a much higher angular resolution of order arcsecs, ($7''$ and $48''$ for the mid- and far-IR instruments, respectively). The *AKARI* survey thus provides the best IR sample for cross-correlation with *Swift* AGN. We use data available in the *AKARI* Point Source Catalogs (*AKARI*/PSC; Ishihara et al. 2010; Yamamura et al. 2010) over a range of wavelengths from $9\text{--}160 \mu\text{m}$. Although *AKARI*'s angular resolution is lower than large ground telescopes (e.g., the diffraction limit of the Very Large Telescope/VISIR $\sim 0.3''$ in the *N*-band), our study has the capability of probing predominantly nuclear emission in the mid-IR (in addition to hard X-rays). This is because torus emission typically dominates over nuclear stellar emission in AGN host galaxies in the wavelength regime of $10\text{--}20 \mu\text{m}$ (e.g., Mor et al. 2009).

The completeness of the base samples (largely unbiased by obscuration) allows us to examine and design various color correlation plots using the hard X-ray and IR powers which can be useful for source classification in blind surveys. Such diagnostics can be particularly powerful if they are redshift independent and can be shown to hold when redshift *K*-correction is accounted for. We propose one such color-color diagnostic, and show that it also provides the capability of distinguishing starbursts from CT AGN. This has been an important problem for many years because star formation and obscured accretion activity often occur together in composite systems (cf. the well known ‘starburst-AGN connection’; e.g., González Delgado et al. 1998; Genzel et al. 1998; Schweitzer et al. 2006; Sanders & Mirabel 1996; Genzel et al. 1998; Malkan et al. 1998; Imanishi et al.

2007). The observed soft X-ray and IR appearance is not easily distinguishable in these cases. Our hard X-ray selection now allows us to do this. The simple photometric diagnostics can be useful tools for new and upcoming hard X-ray surveys with *NuSTAR*, *ASTRO-H* and in the IR with *WISE*.

This paper is organized as follows. In section 2, we present details of the sample selection and catalog cross-matching. Section 3 shows the main results regarding the hard X-ray and IR luminosity correlation and its statistics. Section 4 discusses the implications of the results and provides new diagnostic plots for AGN classification. Section 5 lists the main conclusions. This work is closely related to that of Ichikawa et al. (2012), in which the relation between the IR/X-ray spectra of Seyferts and new type AGN are studied by using the *Swift*/BAT 9-month AGN Catalog (Tueller et al. 2008) and the *AKARI*/PSC complemented by those with *IRAS* and *WISE* to ensure high completeness of cross identification. The larger 22-month BAT sample used as the starting catalog for the present work includes several heavily CT AGN and radio-loud (RL) sources, and we are able to compare the regions occupied by these various AGN classes in the luminosity correlation plane. We also provide detailed statistical tests and correlation fits, and construct AGN photometric classification plots.

A flat Universe with a Hubble constant $H_0 = 71 \text{ km s}^{-1} \text{ Mpc}^{-1}$, $\Omega_{\Lambda} = 0.73$ and $\Omega_{\text{M}} = 0.27$ is assumed throughout this paper.

2. DATA SELECTION

We used the following two all-sky survey catalogs to study the correlation in a complete, flux-limited sample and examine the luminosity correlation between the observed IR and hard X-ray bands of local AGN ($z < 0.1$); the *Swift*/BAT 22-month Source Catalog and the *AKARI*/PSC.

2.1. The *Swift*/BAT 22-month Source Catalog

The prime objective of the *Swift*/BAT is the study of gamma-ray bursts, covering the hard X-ray band of $14\text{--}195 \text{ keV}$. In the 22-month BAT catalog, the total source count is 461 (above a significance of 4.8σ), of which 268 (58%) are AGN. The catalog includes source information of optical counterpart position, X-ray flux, flux error, luminosity, redshift, and AGN type. We adopted the position of the optical counterpart as the source position. The counterpart position error is usually less than $4''$. The detection limit of the catalog is $2.3 \times 10^{-11} \text{ erg cm}^{-2}\text{s}^{-1}$ (for 50% sky coverage). The faintest source included in the catalog has $F_{14\text{--}195 \text{ keV}} = 0.28 \times 10^{-11} \text{ erg cm}^{-2}\text{s}^{-1}$. Although progressively-deeper BAT catalogs are becoming available (e.g., Cusumano et al. 2010), the flux limit of the *AKARI* all sky survey is well-matched for detection of a large fraction of the 22-month X-ray catalog in the infrared, as we show below. Thus, we have restricted ourselves to the 22-month sample for AGN analysis in the present work. We refer to deeper samples only with regard to X-ray emission from starbursts in Section 4.4.3.

The *Swift*/BAT survey produces a long-term average flux, so variability is expected to be partially smoothed over, as compared to large stochastic fluctuations on weekly or monthly timescales. We defined a minimum

flux error of 10%, in order to account for low-order long term variations.

We adopted the spectroscopic AGN types from the BAT catalog for most sources, but for some AGN we checked other works because these source classifications are ambiguous [NGC 235A, NGC 612, ESO 549-G049, NGC 3998, WKK 1263, 4C 50.55, and 3C 445, Véron-Cetty & Véron (2010); NGC 4945, Moorwood et al. (1996); NGC 4992, Bodaghee et al. (2007); Circinus Galaxy, Matt et al. (2000); 3C 345, Unwin et al. (1997)]. We excluded AGN defined as ‘confused and confusing with nearby sources’ in the BAT catalog. Finally, we identified all radio-loud AGN in the combined sample, including type 1 objects such as broad-line radio galaxies and blazars correctly recognized in the BAT classification, and also type 2 sources including narrow-line radio galaxies and low-power FR I radio galaxies which in the BAT catalog are classified simply as Seyfert galaxies (or LINERs) based solely on the characteristics of their optical spectra and regardless of their radio properties.

2.2. The *AKARI* Point Source Catalogs

AKARI has two instruments; the Infrared Camera (IRC) and the Far-infrared Surveyor (FIS). The IRC band centers are 9 and 18 μm , and the FIS band centers are 65, 90, 140, and 160 μm . The *AKARI*/PSC contains the positions and fluxes of 870,973 (IRC) and 427,071 (FIS) sources. In the *AKARI*/PSC, the IRC 80% flux completeness limits are 0.12 and 0.22 Jy, respectively. Also, the FIS 80% completeness corresponds to 3.3, 0.43, 3.6, and 8.2 Jy, respectively. The FIS may be incomplete or show a larger flux error due to detector saturation for sources brighter than ~ 100 Jy. The angular resolution is 7" (IRC) and 48" (FIS), respectively.

In the *AKARI*/PSC, there is a quality flag, *FQUAL*, per band. This flag is a four-level (3-0) flux quality indicator, and the *AKARI* team recommends using only sources with *FQUAL* = 3 for secure scientific analysis. Although sources with *FQUAL* = 2 or 1 may have flux values reported (Yamamura et al. 2010), we used only sources that are confirmed and described by the quality flag *FQUAL*=3, indicating a high reliability of detection and flux accuracy.

2.3. Source identification

We searched for IR counterparts within a 10" radius for the IRC, and 20" radius for the FIS around the position of every optical counterpart listed in the BAT catalog using the *AKARI* Catalog Archive Server (CAS; Yamauchi et al. 2011), which provides user interfaces to search and obtain *AKARI*/PSC information. We adopted these search radii based upon the $\sim 3\sigma$ position uncertainties for each of the *AKARI*/PSC.

We concentrated on three *AKARI* IR bands (9, 18, and 90 μm) throughout this paper because other FIS bands have poorer sensitivities. We summarized the selected source parameters (name, IR fluxes, X-ray luminosity, redshift, AGN type) in Table 1. Additionally, we summarized the total sample statistics for the three *AKARI* bands in Table 2. For the 268 AGN included in the BAT catalog, 158 AGN ($\sim 59\%$) are detected in at least one of the IRC and FIS bands (111 in 9 μm ; 129 in 18 μm ;

113 in 90 μm). These 158 AGN are classified into 81 Seyfert 1 (Sy1) type AGN ($\sim 51\%$, including Seyfert 1, 1.2, and 1.5), 67 Seyfert 2 (Sy2) type AGN ($\sim 42\%$, including Seyfert 1.8, 1.9, and 2), 4 Low-ionization nuclear emission-line regions (LINERs; $\sim 3\%$), and 6 blazars ($\sim 4\%$). Four blazars are flat-spectrum radio quasars (FSRQs), and two are BL Lac objects.

For the purpose of investigating the IR vs. hard X-ray luminosity correlation for various classes of objects, we divide our sample into the following ten categories:

1. “All”
2. “All, ex CT”
3. “Sy1”
4. “Sy1, ex RL”
5. “Sy2”
6. “Sy2, ex CT”
7. “CT”
8. “RL”
9. “Blazar”
10. “RL + Blazar”.

“All” contains all sources detected by the *AKARI* and *Swift*/BAT. “All, ex CT” excludes CT AGN from “All”. “CT” is defined as sources obscured by a gas column density $N_{\text{H}} \geq 1.5 \times 10^{24} \text{ cm}^{-2}$ as measured from X-ray spectroscopy. “Sy1” combines type 1 AGN including radio-quiet objects (Seyferts) and radio-loud sources such as broad-line radio galaxies (BLRGs) and quasars. “Sy1, ex RL” excludes RL AGN from “Sy1”. “Sy2” combines type 2 AGN including CT objects, radio quiet Seyferts, and radio-loud sources such as narrow-line radio galaxies and low-power FR I radio galaxies. “Sy2, ex CT” excludes CT AGN from “Sy2”. “RL” combines all radio-loud AGN in the sample except of blazars, i.e., all radio galaxies of different morphological and spectral types. “Blazar” combines FSRQs and BL Lacs. Finally, “RL + Blazar” merges the two radio loud subsamples.

The criterion of classification as a RL (non-blazar) AGN is that the radio luminosity density at 5 GHz is at least $10^{32} \text{ erg s}^{-1} \text{ Hz}^{-1}$ and the radio to optical *B*-band flux density ratio (R_B) satisfies $\log R_B \geq 1$ (Kellermann et al. 1989; Xu et al. 1999; Molina et al. 2008). RL objects are identified in the final column of Table 1. This list includes 3C and 4C sources from the Cambridge catalogs of radio galaxies, as well as other famous RL sources such as Cen A.

A few additional objects were also identified as RL based on a detailed inspection of the available data and literature. NGC 1052 is a Gigahertz-peaked spectrum (GPS) source, with a spectral peak at 10 GHz (Vermeulen et al. 2003). Although the 5 GHz power is lower than the RL classification threshold, this source displays strong parsec-scale radio emission probably related to newly born jets, and is classified as RL. [HB89]1821+643 is a peculiar radio source, lying at the boundary of the radio-quiet/radio-loud divide (Blundell & Rawlings 2001). The source is a highly luminous quasar in X-rays ($L_{\text{X}} > 1 \times 10^{47} \text{ erg s}^{-1}$; Russell et al. 2010) and lies at the center of a massive galaxy cluster. It shows an FR I like radio morphology (Blundell & Rawlings 2001). As we discuss below, the *AKARI* observations now show that the IR properties of [HB89]1821+643 are consistent with other RL sources, so we include it within the RL classification herein, as

a radio-intermediate (RIM) object. Similarly, two other RIM sources are [HB89]0241+622 (Molina et al. 2008) and Mrk 1501 (Barvainis et al. 2005).

There are several narrow-line Seyfert 1s (NLS1s) in the sample, but these are not distinguishable from the other Seyferts so we do not treat them separately.

3. RESULTS

3.1. Redshift, Flux distribution and Completeness

Figure 1 shows the redshift distribution of the *Swift*/BAT AGN, split into the classes of *AKARI*-detected or non-detected objects. The median redshift of the detected sources (z_{med}) is ≈ 0.0222 , so most are local AGN. There are only 8/158 sources (5%) with $z > 0.1$. The detected source with the maximum redshift is 3C 454.3 ($z_{\text{max}} \approx 0.8590$). The low- z population is dominated by “regular” (radio-quiet) Seyferts, while the high- z population is made mostly from radio-loud AGN (blazars, luminous radio galaxies). The z_{med} for those not detected in any band is $z_{\text{med}} \approx 0.0517$.

Figure 2 shows the hard X-ray flux distribution of the *Swift*/BAT AGN. The X-ray fluxes of the *AKARI* detected sources are higher than the non-detected sources on average. The median X-ray fluxes of the *AKARI* detected/non-detected sources are 5.07/3.38, 4.70/3.36, and $4.70/3.45 \times 10^{-11}$ erg cm $^{-2}$ s $^{-1}$ in 9, 18, and 90 μm , respectively.

Our cross-correlation between the all-sky X-ray and IR samples is about 60% complete, with the X-ray sources non-detected in the IR being fainter than the detected ones, on average. It has been shown by Ichikawa et al. (2012) that supplementing the *AKARI* data with the deeper *WISE* samples maintains the luminosity correlation. Overall, none of the statistical inferences presented in the sections below should be affected by incompleteness of the cross-matching.

3.2. Hard X-ray to IR luminosity correlation

Figure 3 shows the luminosity correlation for the detected sources between hard X-ray (14–195 keV) and IR (9, 18, and 90 μm) bands. We find that there is a strong linear correlation for most AGN between the logarithms of the observed IR and hard X-ray luminosities over four orders of magnitude. Here, we calculated the absolute luminosities by using the redshift listed in the BAT catalog (Tueller et al. 2010). In principle, K -correction may become important for high- z objects, e.g., blazars. Our samples are mainly local AGN, but blazars ($z = 0.0533$ – 0.8590) are also included. If we apply K -correction to AGN at $z \sim 0.9$, the maximum effect for L_X is $\sim 10\%$ assuming a power law spectrum with a photon index of $\Gamma \sim 1.9$, which is a typical value for the majority of AGN in our sample. This is a small effect especially when comparing logarithmic luminosities, so we did not apply any K -corrections.

We tested the luminosity correlation by using the algorithm of Isobe et al. (1990), which is used when the nature of the scatter of points in a correlation is ill understood. We computed the linear regression coefficients by one of the methods of the algorithm, “OLS bisector”, recommended if the goal is to determine the functional relation between the two axes. The formula is given by

$$\log L_{\text{IR}} = a + b \log L_X, \quad (1)$$

where L_{IR} and L_X are observed luminosities in IR (9, 18, and 90 μm) and hard X-ray (14–195 keV). The variables a and b are the intercept and slope of the fitting result, respectively. At 9 μm , the luminosity correlation of the subsample “Sy1” is described as

$$\log\left(\frac{\lambda L_{9\mu\text{m}}}{10^{43} \text{ erg s}^{-1}}\right) = (0.15 \pm 0.05) \\ + (0.94 \pm 0.06) \log\left(\frac{L_X}{10^{43} \text{ erg s}^{-1}}\right). \quad (2)$$

The fit parameters for other bands are listed in Table 3, and are plotted in Figure 3 along with the 1σ and 2σ uncertainties on the correlation normalization. Also, we summarize the fitting results with respect to various subsamples in Table 3.

We checked two correlation coefficients for every subsample, the Spearman’s Rank correlation coefficient (ρ) and the partial correlation coefficient (ρ_z). The ρ and ρ_z correlation tests return values in the interval $[-1.0, 1.0]$. The ρ_z statistic is especially important because artificial correlations between luminosities may be induced in a flux limited-sample even in the absence of any intrinsic correlation, but the partial correlation coefficient can account for this by excluding the effect of redshift. A large value implies a significant positive, linear correlation. These test coefficients values are also listed in Table 3.

“Blazar” and “RL + Blazar” typically show very high values of ρ and ρ_z in all three *AKARI* bands. But only a handful of objects included in both subsamples are among the most luminous and distant sources in the entire sample considered, so the correlation results for these may be biased by small number statistics and flux limits. The ρ and $\rho_z = 1$ values in these cases must be treated with caution. The other subsamples with the highest values of ρ and ρ_z are the “Sy1” and “All, ex CT” subsamples. “Sy2” also show a correlation, if CT sources are excluded, though somewhat weaker than “Sy1”. CT sources will be discussed separately in section 4.2. The correlation coefficients generally decrease towards longer IR wavelengths.

4. DISCUSSION

4.1. Mid-infrared to hard X-ray correlation for Seyfert AGN

Based upon a detailed comparison of the complete, flux-limited *AKARI* and *Swift*/BAT all-sky surveys, we have found a good linear correlation for Seyfert AGN between the logarithms of the observed mid-IR and hard X-ray luminosities over four orders of magnitude (Figure 3). The correlation persists despite the fact that no corrections have been performed for obscuration or reddening, nor for any contamination by host galaxy emission. The selected surveys thus provide insight into the nature of mid-IR and X-ray populations of sources selected from all-sky data in a completely unbiased fashion. Statistical tests accounting for redshift effects show that there is definite intrinsic correlation in the two energies for various classes of AGN.

Hard X-ray emission is produced very near the black hole. The soft-to-hard X-ray emission of Seyfert AGN is produced by successive Compton scatterings of the thermal UV photons emitted by accretion disks in hot,

most likely patchy coronae formed above the disks (e.g., Haardt & Maraschi 1993). The high-energy disk and corona emission also heat dusty tori located at further distances from the centers, where the nuclear UV-to-X-ray continuum is re-processed into the thermal IR photons. It is widely accepted that the observed radiative output of Seyfert galaxies at mid-IR frequencies is dominated by the torus emission, which, at least in the case of unobscured (type 1) sources, may even extend up to the near-IR range due to the hot dust located near the dust sublimation radius at the outer edge of the accretion disk (e.g., Elitzur 2008). In this scenario, our result of the good linear correlation for Seyfert AGN between the observed mid-IR and hard X-ray represents well the view of the unified schemes for Seyfert AGN (Antonucci 1993).

The best-fit correlation lines for Sy1s (where we have a direct view of the nuclear regions in both X-rays and IR) are plotted in Figure 3 and are used as the benchmark for comparison again among various source classes in the following sections. It is important to note that the correlation when fitting to the sample of “All” AGN, is quite similar to the benchmark “Sy1” sample, which means that these correlations provide an easy route for conversion between IR and hard X-ray powers irrespective of source class. If the type of some newly-identified AGN were not known, direct use of the best fit parameters for the “All” sample could still be used to convert between X-ray and IR powers, to within the accuracy provided by the correlation scatter.

The dispersion in these correlations is $\sim 0.3\text{--}0.5$ dex (cf. σ_r values in Table 3). The strength of the correlation decreases towards longer wavelengths (lower ρ and ρ_z) in conjunction with increasing σ_r values. This may be explained by an increasing host galaxy contribution with wavelength, resulting in a large IR spread.

It should be noted that although dominated by torus emission in the mid-IR, *AKARI*'s beam will encompass a stronger host galaxy contribution as opposed to observations with large ground-based telescopes. This manifests itself as slightly flatter best-fit correlation slopes as compared to the previously-measured correlation using VLT data by Gandhi et al. (2009, with the caveat that their sample was much smaller). The slopes we now find for the non-CT radio quiet Seyferts in Table 3 range over b ($9\ \mu\text{m}$) $\approx 0.92\text{--}0.99$, as compared to the previously measured value of $b = 1.02$ using the same OLS bisector fit statistic. The host galaxy contribution is relatively stronger for lower luminosity AGN, as a result of which their total observed *AKARI* fluxes are systematically biased towards the right (to higher IR powers) in Figure 3, thus flattening the correlation (Vasudevan et al. 2010; Mullaney et al. 2011). The effect is small at luminosities of $L_X > 10^{43}$ erg s^{-1} and above where most of the BAT AGN lie (see, e.g., Eq. 1 of Vasudevan et al. 2010), hence the marginal difference in slopes. We do not subtract any star formation contribution here because this introduces model dependencies, and our aim is to define the correlation properties and source classification diagnostics in *observed* space, such that they may be useful for future surveys for unclassified objects. Ideally, an all-sky infrared survey with 8–10 m telescopes ought to be carried out in the near future; this would combine the

best angular resolution with complete sample selection.

In summary, a significant correlation is observed between the hard X-ray and various IR bands for Sy1 and Sy2. The correlation is intrinsic to the source fluxes and is a useful empirical tool for converting between the two energies.

4.2. Mid-infrared to hard X-ray correlation for Compton-thick AGN

The only class of AGN which does not show any correlation between the two bands is that of CT AGN, with ρ_z values near zero (Table 3). Including CT sources within the class of “Sy2” results in a decrease of the Sy2 correlation as well. We referred to Table 8.1 in Comastri (2004) and other recent results about CT AGN, preferring those based upon observations carried out above 10 keV with *BeppoSAX*, *Suzaku*, and *Swift*/BAT. We identified nine CT AGN from our sample. Their properties and relevant literature are listed in Table 4.

Gandhi et al. (2009) showed that the mid-IR-to-X-ray correlation for CT AGN is almost indistinguishable from that of typical Seyferts, when the X-ray luminosities are corrected for obscuration. The difference here is that we are using observed hard X-ray fluxes and converting them to luminosities without absorption-correction. While absorption does not affect the *Swift*/BAT energy band for Compton-thin column densities, down scattering does deplete hard X-ray photons when the column becomes CT (e.g., Ikeda et al. 2009). Our sample contains a range of obscuring column densities, including one AGN with an extreme column of $N_H > 10^{25}$ cm^{-2} (the CT sources are listed in Table 4). This leads to an absence of any correlation for our relatively-small sample of CT AGN. As we discuss in the next section, the hard X-ray deficit is useful for isolating CT sources.

4.3. Mid-infrared to hard X-ray correlation for radio-loud AGN

4.3.1. Radio-loud AGN

RL AGN follow a good linear correlation between the logarithms of mid-IR and hard X-ray luminosities (Figure 3). A correlation is also present in flux–flux space as seen by the high ρ_z ($= 0.89$) for the “RL” sample in Table 3 in all three *AKARI* bands. The correlation slopes of the RL sample match those of Sy 1s within 1σ uncertainties. The above similarity suggests that the hard X-ray and IR emission processes of RL AGN are similar to Seyferts. RL AGN probed by *Swift*/BAT lie at higher redshifts than Seyferts ($z_{\text{med}} \approx 0.052/0.019$). But their flux distributions, and in particular, the infrared-to-X-ray flux ratios, are very similar to Seyferts ($R_{\text{med}} = 1.0 \pm 0.1/1.2 \pm 0.2$), where $R = \text{flux}_{9\mu\text{m}}/\text{flux}_{\text{X-ray}}$.

The scatter in the correlation, on the other hand, is larger for the RL sample in all bands. This can be seen in Figure 3 as resulting from a few outliers. In all bands, the sources with the largest offset towards higher X-ray luminosities (i.e., those lying *above* the correlation) are type 1 RL AGN or blazar sources. The sources that lie above the 2σ uncertainty of the luminosity correlation for “Sy1” are radio galaxies with particularly powerful jets 3C 111.0, 4C 50.55, and radio-loud quasar 3C 273 in 9, 18, and 90 μm , respectively.

The origin of the broadband emission of radio galaxies

is a matter of considerable debate. With regard to the origin of X-ray emission, Evans et al. (2006) demonstrate that both accretion and jet-related components may be present in all radio galaxy nuclei, with the larger contribution of accretion in more luminous population and vice-versa. Hardcastle et al. (2009) found a good correlation between mid-IR ($15\ \mu\text{m}$, *Spitzer*) and accretion-related X-ray luminosities (in 2–10 keV, *Chandra* and *XMM-Newton* bands) in their sample of 135 radio galaxies. This suggests that the mid-IR emission is mainly from dusty torus and is not strongly affected by jet beaming, especially in the case of luminous sources with intrinsic X-ray powers above $\sim 10^{43}\ \text{erg s}^{-1}$ similar to the range of luminosities that we are probing. This is also supported by mid-IR spectroscopic analysis of luminous RL AGN (Leipski et al. 2010), and finally, is also borne out by the similar mid-IR appearance of radio-quiet and radio-loud quasars in the composite spectra assembled by Elvis et al. (1994).

Hardcastle et al. (2009) did note that quasars and BLRG in their sample tended to have higher X-ray luminosities than the low-power radio galaxies of similar IR luminosity, suggesting that the X-ray powers of brighter sources can be more severely contaminated by jet emission. Our observed outliers appear to show similar X-ray excesses, so we examined published detailed X-ray spectroscopic results for these AGN to gain further insight. The X-ray spectra of 3C 111.0 obtained with *Suzaku* indeed showed jet dominant component in the hard X-ray band, as found by Ballo et al. (2011). On the other hand, in the broadband X-ray spectra of 4C 50.55 determined by *Suzaku* and *Swift*/BAT data, there is little jet contribution to hot coronal Comptonization (Tazaki et al. 2010). 3C 273 will be discussed in the next section. It is interesting to note that both 3C 111.0 and 4C 50.55 belong to the class of BLRG, which was the only class for which Sambruna et al. (1999) identified some systematic differences in X-ray spectral slope (albeit weak) with respect to radio quiet AGN. On the other hand, other BLRGs such as 3C 120 (Kataoka et al. 2007) are not largely offset from our correlation.

In summary, we lack conclusive evidence of any strong and systematic differences for our RL samples as a whole, though some jet contribution (and related excess variability) may explain slight offsets in the IR–X-ray correlation plane for some objects. In any case, RL sources join on to the luminous end of the sample of Seyferts and extend the observed correlation in that regime.

4.3.2. Blazars

The broadband spectra of blazars are thought to be dominated by non-thermal emission from their relativistic jets (Bregman 1990; Fossati et al. 1998). The IR regime of FSRQs is mainly synchrotron radiation, and hard X-rays are from the inverse-Compton scattering of soft target photons produced either within the jet (synchrotron self-Compton process) or external to the jet (e.g., within the broad emission line region or dusty tori). In the case of low-power BL Lacs, X-rays are typically dominated by the high-energy tail of the synchrotron continuum. Such “high frequency-peaked” BL Lacs are however absent in our BAT/*AKARI* sample. Other components including accretion disk and host galaxy emission are present in most sources at a weaker level (e.g.,

Abdo et al. 2010). Whether or not a torus contributes to the IR emission is debated, but it is generally found to be present more often in luminous FSRQ sources than in BL Lac (e.g., Malmrose et al. 2011; Plotkin et al. 2011).

Our blazar sample contains four FSRQs and two BL Lac. Although the sample size is small, we find high values for partial correlation coefficients between the IR and hard X-ray fluxes for blazars ($\rho_z \approx 0.8 - 0.9$ in 9 and $18\ \mu\text{m}$; see Table 3). This is expected if the various synchrotron and inverse Compton components are intrinsically correlated. On the other hand, the apparent observation from Figure 3 that blazars extend the Sy1 correlation is likely to be a coincidence. This is because the correlation implies a near 1:1 absolute normalization (i.e., mid-IR luminosities are very similar to the hard X-ray powers), which may be explained according to the ‘blazar sequence’ of Fossati et al. (1998). Figure 12 of their work shows that the *AKARI* ($9\ \mu\text{m}$) and *Swift*/BAT (14–195 keV) bandpasses sample similar power levels at all luminosities, to within a factor of a few at most. Furthermore, Malmquist bias certainly contributes to the luminosity-to-luminosity correlation in flux-limited samples for objects spanning a limited flux range but a large redshift range (e.g., Antonucci 2011), which is true in the case of BAT-selected blazars. A larger flux range needs to be sampled before detailed conclusions on the origin and validity of the correlation for blazars may be drawn.

Amongst blazars, the FSRQ 3C 273 shows the strongest mismatch between the observed hard X-ray and IR powers (lying on or well above the 2σ Sy correlation lines in Figure 3). This object is known to show strong multi-component variability (e.g., Courvoisier et al. 1987), which may account for its position in the IR-to-X-ray plane.

In summary, results from the above two sections imply that our IR-to-X-ray correlation may be used to predict and convert between the mid-IR and hard X-ray powers of RL AGN, in addition to Seyferts. The hard X-ray/IR-brightest blazars included in our flux-limited sample happen to lie along this correlation as well, which is likely to be a coincidence and not an indication for the presence of dust. Thus, the IR vs. X-ray correlation is a useful empirical tool irrespective of the underlying emission physics. This is confirmed by the fact that when we gather all Compton-thin AGN together, irrespective of radio classification, large positive values of ρ_z are found (see “All, ex CT” subsample in Table 3).

4.4. Photometric diagnostics for source classification

Photometric diagnostics for identifying various source classes (e.g., by using observed power or flux ratios between various bands) can be simple and powerful observational tools. Unbiased all-sky surveys such as ours are ideal for testing various classification schemes, which may be applied to large blind surveys, and we have carried out such a search. The IR-to-X-ray correlations for Sy1, Sy2, and LINERs closely match each other (Gandhi et al. 2009; Asmus et al. 2011). Here, we investigate to what extent Seyferts, RL AGN, and CT sources may be separated using the mid-IR and hard X-ray correlations.

4.4.1. Radio-loud AGN

As already mentioned, RL AGN (and blazars, with the aforementioned caveats) follow the same correlation as Seyferts in Figure 3. But these sources lie at the high luminosity end on both axes. RL AGN can also be separated by using a luminosity vs. flux ratio (L_X vs. $\lambda L_{\lambda(9\mu\text{m})}/\lambda L_{\lambda(90\mu\text{m})}$) plot, equivalent to an absolute magnitude vs. color diagram. The result is shown in Figure 4. Non-detected RL AGN were included by using IRC 9 μm and FIS 90 μm detection limits of 0.12 and 0.55 Jy, respectively.

Most Seyferts show a large spread in the mid-IR-to-far-IR ratio with an average value of $\lambda L_{\lambda(9\mu\text{m})}/\lambda L_{\lambda(90\mu\text{m})} = 1.03$. Type 1 RL AGN and blazars, on the other hand, occupy the region of high hard X-ray emission and high mid-IR-to-far-IR ratio as compared to other AGN types. Using approximate boundaries of $\log L_X > 44.3$ and $\lambda L_{\lambda(9\mu\text{m})}/\lambda L_{\lambda(90\mu\text{m})} > 1$ for the box shown in the figure, we find that *all* type 1 RL AGN and blazars lie in this region, i.e., selection is 100% *complete*. On the other hand, the box also contains a few (2/16) sources that are neither type 1 RL AGN nor blazars, i.e., selection is 88% *reliable*. If we classify [HB89]0241+622 and [HB89]1821+643 as radio-quiet (see discussion in section 2.3), the reliability drops to 75%.

On the other hand, type 2 RL AGN are not clearly separated in this figure. In particular, they show a lower ratio of the mid- to far-IR powers on the ordinates-to-the median values for $\lambda L_{\lambda(9\mu\text{m})}/\lambda L_{\lambda(90\mu\text{m})}$ for type 1 RL and type 2 RL are 0.31 and -0.11, respectively. This trend is also seen in the case of the radio-quiet sources (RQ), with the corresponding ratios being 0.16 and -0.16 for type 1 RQ and type 2 RQ, respectively. This trend cannot arise from optically-thick tori in Sy2 being preferentially ‘colder’ in the infrared. If this were so, then Sy2 would also be offset towards lower 9 μm -to-X-ray flux ratios in the IR-to-X-ray correlations. Instead, this trend probably arises because Sy2 have lower intrinsic accretion (X-ray) luminosities as compared to Sy1 on average (Winter et al. 2009), as well as a relatively stronger 90 μm contribution from dust in the host galaxy (Malkan et al. 1998). These two facts push down the 9 μm fluxes for Sy2 and boost their 90 μm fluxes, resulting in the observed trend.

With regard to the fact that blazars occupy the top right of Figure 4, an x-axis mid-to-far-IR luminosity ratio greater than 1 means that their jet synchrotron peaks must lie in the mid-IR or higher frequencies and not the far-IR or lower frequencies. This is interestingly consistent with the recent study of bright blazars detected at GeV photon energies by *Fermi*/LAT (Abdo et al. 2010), where no source with the synchrotron continuum peaked at far-IR or lower frequencies was found. Further investigation is beyond the scope of this paper and is left to future work.

Finally, it is seen from Figure 4 that there are no luminous X-ray sources with a mid-IR-to-far-IR ratio of less than 1 occupying the top left of the diagram. Type 2 quasars with powerful X-ray emission and bright host galaxies probably occupy this region, but these are known to be elusive and absent in the local universe (e.g., Zakamska et al. 2003; Gandhi et al. 2004, 2006). We also note that we would not have selected sources that are below the *AKARI* detection limit in both 9 and 90 μm . Since our sample contains very few blazars, a selection

bias where we miss such sources cannot be ruled out.

In summary, Figure 4 is helpful for isolating type 1 RL AGN and blazars. Using color and luminosity information we can isolate type 1 RL AGN with high reliability, but this requires knowledge of source redshift.

4.4.2. Compton-thick AGN

Outliers in the correlation plots of Figure 3, which lie *below* the correlation for “Sy1”, are mostly CT AGN. Their average $L_X/\lambda L_{\lambda(9\mu\text{m})}$ ratio is 0.11, as compared to 0.71 for Sy1. When generating such correlation plots, it is important to use the observed X-ray flux for identifying CT AGN because of the hard X-ray deficit due to Compton down-scattering (Sec. 4.2).

The average values of the X-ray-to-IR ratios for other *AKARI* bands are $L_X/\lambda L_{\lambda(18\mu\text{m})} = 0.08$ and $L_X/\lambda L_{\lambda(90\mu\text{m})} = 0.03$. Copious star formation often accompanies obscured AGN activity and several of the CT AGN lie in composite systems also classified as starburst galaxies (e.g., NGC 6240, Circinus Galaxy, NGC 4945. See Table 4). The 90 μm to X-ray ratio for CT AGN is large because of an excess far-IR contribution due to bright star formation in the host galaxy (see also Figure 3).

4.4.3. Distinguishing between Compton-thick AGN and Starburst galaxies

The difficulty of distinguishing heavily obscured AGN in composite systems from pure starburst galaxies has been an important problem for many decades (e.g., Genzel et al. 1998; González Delgado et al. 1998; Schweitzer et al. 2006). X-ray information only below 10 keV has been used in most surveys so far. But the observed X-ray fluxes for both these classes of sources in this band are low as compared to their observed IR fluxes. Thus, such sources are often indistinguishable photometrically. High excitation mid-IR forbidden lines and PAHs can separate the two (e.g., Laurent et al. 2000; Sturm et al. 2002; Dale et al. 2006; Goulding & Alexander 2009; Weaver et al. 2010), if spectroscopic data are available.

We now have new information available from the hard X-ray band above 10 keV. We investigate whether the information is useful for source classification. We checked the hard X-ray emission of starburst galaxies. There is no starburst galaxy detected in the 22-month BAT catalog, so we have extended our search to the 54-month BAT catalog (Cusumano et al. 2010) for this purpose. The detection limits of the 54-month catalog are 1.0×10^{-11} ($|b| < 10^\circ$) and 9.2×10^{-12} erg cm $^{-2}$ s $^{-1}$ ($|b| > 10^\circ$), respectively. M82 is the only “pure” starburst galaxy detected in this catalog.

Though only one starburst galaxy is detected, hard X-ray predictions on other well-known sources turn out to be interesting for our purpose of comparison with AGN. We picked up two famous “pure” starburst galaxies (NGC 253, Arp 220), and other four “pure” starburst galaxies (NGC 2146, NGC 3256, NGC 3310, and NGC 7714) listed in Brandl et al. (2006), which are all detected in X-rays below 10 keV. We computed hard X-ray flux estimates for these 6 objects by using their observed 2–10 keV fluxes under the two different assumptions of non-thermal and thermal radiation models (The

results are listed in Table 5). These correspond to the emission expected from point sources like X-ray binaries and diffuse thermal gas, respectively (Persic & Rephaeli 2002). The non-thermal model is based upon the observation of star-forming galaxies in the Hubble Deep Field with an average 2–10 keV X-ray spectral slope (photon index $\Gamma = 2.1$; Ranalli et al. 2003). The thermal model (7 keV APEC) is based on the *XMM-Newton* observation of the central region of M82 (Ranalli et al. 2008). Similar starburst-related hot gas bubbles have also been found in Arp 220 (Iwasawa et al. 2005) and NGC 253 (Pietsch et al. 2001).

Because M82 and NGC 253 are very bright in the IR (≥ 100 Jy), the *AKARI* detectors may cause saturation and the flux could have larger uncertainty (Yamamura et al. 2010). The FIS 90 μm fluxes of these two sources are not reliable ($FQUAL = 1$), and there is no IRC 9 μm flux available for M82 in the all-sky survey. Therefore we applied the results of the *AKARI* pointed observation data for M82 (Kaneda et al. 2010) and NGC 253 (Kaneda et al. 2009). In these observations, the IRC and FIS were operated in special observation mode, which is used to observe bright sky regions to avoid detectors saturation.

Figure 5 shows the results in the form of a $\log L_X/\lambda L_{\lambda(9\mu\text{m})}$ vs. $\log \lambda L_{\lambda(9\mu\text{m})}/\lambda L_{\lambda(90\mu\text{m})}$ diagram (equivalent to a color-color plot). We also include an IR color lower limit for the CT AGN, NGC 4945, resulting from it being saturated in the FIS (~ 100 Jy). Other CT AGN non-detected at 9 μm are also included as limits. Considering the AGN only, an approximate boundary of $\log L_X/\lambda L_{\lambda(9\mu\text{m})} < -0.9$ successfully isolates CT AGN, i.e., it has very high (100%) reliability. But only 5/8 of CT sources are below this boundary, which means that it is 56% complete. This boundary can successfully identify CT sources, if a source is known to contain an AGN a priori.

But such a priori information is not available for most surveys, and we see from the figure that starburst galaxies also occupy this region. Starburst galaxies (including the single detection of M82 and virtually all prediction ranges) are all concentrated below the line of $\log L_X/\lambda L_{\lambda(9\mu\text{m})} \sim -2.5$. For each source, a vertical line connects the expected range of values based upon the non-thermal model for the X-ray emission (higher horizontal bar) and the thermal model (lower horizontal bar). This shows that the hard X-ray emission from starburst galaxies is expected to be less than $\sim 10^{-3}$ of the mid-IR emission from AGN.

The abscissa, $\log \lambda L_{\lambda(9\mu\text{m})}/\lambda L_{\lambda(90\mu\text{m})}$, shows the ratio of hot-to-cool dust. Starburst galaxies are largely separated on the abscissa as well because of cooler dust temperature compared to AGN. We also tested the ratio of 15 other “pure” starburst galaxies listed in Brandl et al. (2006), and obtained an upper limit of $\log \lambda L_{\lambda(9\mu\text{m})}/\lambda L_{\lambda(90\mu\text{m})} \sim -0.4$. The result shows that the far-IR emission from the cool dust is more dominant than the mid-IR emission from hot dust in the local starburst galaxies.

On the other hand, RL AGN are not separated out in this figure. 3C 111 and 3C 273 lie towards the top right region in the plot (again 3C 111 has the largest $\log L_X/L_{\text{IR}}$ ratio), so it might be possible to define some

region here, but in general RL AGN and blazars do not occupy any specific region.

In summary, the hard X-ray and IR color-color plot successfully differentiates the composite CT AGN/starburst galaxies, and also distinguishes these from the remaining sources (Sy1, Sy2, LINERs, and RL AGN).

4.4.4. *K*-corrections in the color-color plane

In order to be useful for general source classification, the regions determined in the previous section must be shown to accommodate the effect of SED *K*-corrections at higher redshifts. We checked this by applying *K*-correction for template SEDs of Seyferts, CT AGN, and starburst galaxies separately. For Seyferts, we use the high-luminosity starburst model spectrum ($L = 10^{13} L_{\odot}$) by Lagache et al. (2003). For CT AGN and starburst galaxies, we use the Seyfert 2 and M82 model spectra, respectively, by Polletta et al. (2007). We show the color tracks on the plane of Figure 5 when the redshift is varied from $z = 0.0$ to 4.0. We assumed a color-color position of (0, 0) for the local origin of the *K*-correction locus for Seyferts. Similarly, the loci of CT AGN and starburst galaxies start at the positions of Circinus Galaxy and M82, respectively. The plotted loci show that our diagnostic regions are independent of source redshift.

With current and upcoming hard X-ray missions of continually improving sensitivity (e.g., *INTEGRAL*, *Swift*, *NuSTAR*, *eROSITA*, and *ASTRO-H*), and similar increases in sensitivity expected in the IR (e.g., *WISE* and *SPICA*), our work investigates the degree to which blind IR/X-ray surveys can be used for classification and separation of AGN and starburst galaxies, using directly observed photometric properties without the requirement of detailed spectroscopy or source modeling. For instance, changing from the *Swift*/BAT 14–195 keV and *AKARI* 9 μm bands to the *NuSTAR* 6–79 keV and *WISE* 12 μm bands, respectively, the maximal shift in the ordinates of the color-color plane is only $\sim 20\%$ towards lower L_X , for a Seyfert SED at $z \sim 4$.

5. CONCLUSIONS

We have combined two complete, flux-limited all-sky surveys, *AKARI* and *Swift*/BAT, in order to study the connection between the IR and hard X-ray (> 10 keV) bands for AGN. We found a good linear correlation between the logarithms of the observed mid-IR and hard X-ray luminosities over four orders of magnitude. Under the AGN orientation-based unification scheme, this result may be viewed as supporting clumpy torus models, although the broad-band correlation alone cannot prove the underlying emission mechanism for the IR and hard X-ray bands. We also found that all the RL AGN follow a good linear correlation, suggesting that their dominant hard X-ray and IR emission processes are similar to those of radio-quiet sources. Coincidentally, blazars also possess a near 1:1 intrinsic correlation between the two bands, which is due to the fact that the synchrotron and inverse Compton powers match each other well along the blazar sequence. We present quantitative correlation statistics and show that artificial redshift effects do not dominate the correlation for Seyferts nor for RL AGN. The correlation fits are a useful empirical tool for observers. Most CT AGN show a large deficit in their ob-

served X-ray powers compared to unobscured AGN. This is expected because their observed fluxes are diminished by high gas column densities, even in the hard X-ray band.

We investigated hard X-ray and IR photometric diagnostics for source classification. We could isolate type 1 RL AGN and blazars by using absolute magnitude vs. color diagram such as $\log L_X$ vs. $\lambda L_{\lambda(9\mu\text{m})}/\lambda L_{\lambda(90\mu\text{m})}$. Using approximate boundaries of $\log L_X > 44.3$ and $\lambda L_{\lambda(9\mu\text{m})}/\lambda L_{\lambda(90\mu\text{m})} > 1$, we found that *all* type 1 RL AGN and blazars lie in this region with a reliability of 88%. The optical Seyferts classification is related to the 9 vs. 90 μm infrared flux ratio with type 2 sources showing a lower ratio than type 1. We discussed biases resulting from our flux limited selection and the absence of rare populations such as type 2 quasars in the present, local sample.

We also found that the color-color plot of $\log L_X/\lambda L_{\lambda(9\mu\text{m})}$ vs. $\log \lambda L_{\lambda(9\mu\text{m})}/\lambda L_{\lambda(90\mu\text{m})}$ is able to

distinguish starburst galaxies and composite CT sources from other normal AGN. We defined several boundaries, which can be used for reliable and complete source classification. CT AGN are successfully isolated by the approximate boundary of $\log L_X/\lambda L_{\lambda(9\mu\text{m})} < -0.9$ with very high (100%) reliability amongst AGN, but completeness of 56%. Starburst galaxies are isolated in a region with approximate boundary of $\log L_X/\lambda L_{\lambda(9\mu\text{m})} < -2.5$ and $\log \lambda L_{\lambda(9\mu\text{m})}/\lambda L_{\lambda(90\mu\text{m})} < -0.4$ and very high (100%) reliability.

We acknowledge the work of the *AKARI*/PSC and the *Swift*/BAT 22-month Source Catalog teams. We also acknowledge the referee for constructive comments and suggestions. This work was partly supported by the Grant-in-aid for Scientific Research 20740109, 21244017 (YT), and 23540265 (YU) from the Ministry of Education, Culture, Sports, Science, and Technology of Japan.

REFERENCES

- Abdo, A. A., Ackermann, M., Agudo, I., et al. 2010, *ApJ*, 716, 30
- Antonucci, R. 1993, *ARA&A*, 31, 473
- Antonucci, R. 2011, arXiv:1101.0837
- Asmus, D., Gandhi, P., Smette, A., Hönig, S. F., & Duschl, W. J. 2011, arXiv:1109.4873
- Ballo, L., Braito, V., Reeves, J. N., Sambruna, R. M., & Tombesi, F. 2011, arXiv:1108.2609
- Barvainis, R., Lehár, J., Birkinshaw, M., Falcke, H., & Blundell, K. M. 2005, *ApJ*, 618, 108
- Bauer, M., Pietsch, W., Trinchieri, G., Breitschwerdt, D., Ehle, M., Freyberg, M. J., & Read, A. M. 2008, *A&A*, 489, 1029
- Blundell, K. M., & Rawlings, S. 2001, *ApJ*, 562, L5
- Bodaghee, A., et al. 2007, *A&A*, 467, 585
- Brandl, B. R., et al. 2006, *ApJ*, 653, 1129
- Bregman, J. N. 1990, *A&A Rev.*, 2, 125
- della Ceca, R., Griffiths, R. E., Heckman, T. M., Lehnert, M. D., & Weaver, K. A. 1999, *ApJ*, 514, 772
- Comastri, A. 2004, *Supermassive Black Holes in the Distant Universe*, 308, 245
- Comastri, A., Iwasawa, K., Gilli, R., Vignali, C., Ranalli, P., Matt, G., & Fiore, F. 2010, *ApJ*, 717, 787
- Courvoisier, T. J.-L., et al. 1987, *A&A*, 176, 197
- Cusumano, G., et al. 2010, *A&A*, 524, A64
- Dale, D. A., Smith, J. D. T., Armus, L., et al. 2006, *ApJ*, 646, 161
- Diamond-Stanic, A. M., Rieke, G. H., & Rigby, J. R. 2009, *ApJ*, 698, 623
- Dullemond, C. P., & Dominik, C. 2005, *A&A*, 434, 971
- Elitzur, M. 2008, *NewAR*, 52, 274
- Elvis, M., et al. 1994, *ApJS*, 95, 1
- Evans, D. A., Worrall, D. M., Hardcastle, M. J., Kraft, R. P., & Birkinshaw, M. 2006, *ApJ*, 642, 96
- Fossati, G., Maraschi, L., Celotti, A., Comastri, A., & Ghisellini, G. 1998, *MNRAS*, 299, 433
- Gandhi, P., Crawford, C. S., Fabian, A. C., & Johnstone, R. M. 2004, *MNRAS*, 348, 529
- Gandhi, P., Fabian, A. C., & Crawford, C. S. 2006, *MNRAS*, 369, 1566
- Gandhi, P., Horst, H., Smette, A., Hönig, S., Comastri, A., Gilli, R., Vignali, C., & Duschl, W. 2009, *A&A*, 502, 457
- Genzel, R., et al. 1998, *ApJ*, 498, 579
- González Delgado, R. M., Heckman, T., Leitherer, C., Meurer, G., Krolik, J., Wilson, A. S., Kinney, A., & Koratkar, A. 1998, *ApJ*, 505, 174
- González-Martín, O., et al. 2011, *A&A*, 527, A142
- Goulding, A. D., & Alexander, D. M. 2009, *MNRAS*, 398, 1165
- Hönig, S. F., Beckert, T., Ohnaka, K., & Weigelt, G. 2006, *A&A*, 452, 459
- Hönig, S. F., Kishimoto, M., Gandhi, P., et al. 2010, *A&A*, 515, A23
- Hönig, S. F., & Kishimoto, M. 2010, *A&A*, 523, A27
- Haardt, F., & Maraschi, L. 1993, *ApJ*, 413, 507
- Hardcastle, M. J., Evans, D. A., & Croston, J. H. 2009, *MNRAS*, 396, 1929
- Horst, H., Smette, A., Gandhi, P., & Duschl, W. J. 2006, *A&A*, 457, L17
- Horst, H., Gandhi, P., Smette, A., & Duschl, W. J. 2008, *A&A*, 479, 389
- Horst, H., Duschl, W. J., Gandhi, P., & Smette, A. 2009, *A&A*, 495, 137
- Ichikawa, K., Ueda, Y., Terashima, Y., Oyabu, S., Gandhi, P., Matsuda, K., & Nakagawa, T., 2012, *ApJ*, submitted
- Ikeda, S., Awaki, H., & Terashima, Y. 2009, *ApJ*, 692, 608
- Imanishi, M., Dudley, C. C., Maiolino, R., Maloney, P. R., Nakagawa, T., & Risaliti, G. 2007, *ApJS*, 171, 72
- Ishihara, D., et al. 2010, *A&A*, 514, A1
- Isobe, T., Feigelson, E. D., Akritas, M. G., & Babu, G. J. 1990, *ApJ*, 364, 104
- Itoh, T., et al. 2008, *PASJ*, 60, 251
- Iwasawa, K., Sanders, D. B., Evans, A. S., Trentham, N., Miniutti, G., & Spoon, H. W. W. 2005, *MNRAS*, 357, 565
- Iyomoto, N., Fukazawa, Y., Nakai, N., & Ishihara, Y. 2001, *ApJ*, 561, L69
- Joint *IRAS* Science, W. G. 1994, *VizieR Online Data Catalogue*, 2125, 0
- Kataoka, J., Reeves, J. N., Iwasawa, K., et al. 2007, *PASJ*, 59, 279
- Kaneda, H., Yamagishi, M., Suzuki, T., & Onaka, T. 2009, *ApJ*, 698, L125
- Kaneda, H., et al. 2010, *A&A*, 514, A14
- Kellermann, K. I., Sramek, R., Schmidt, M., Shaffer, D. B., & Green, R. 1989, *AJ*, 98, 1195
- Krolik, J. H., & Begelman, M. C. 1988, *ApJ*, 329, 702
- Krabbe, A., Böker, T., & Maiolino, R. 2001, *ApJ*, 557, 626
- Leipski, C., Haas, M., Willner, S. P., et al. 2010, *ApJ*, 717, 766
- Lagache, G., Dole, H., & Puget, J.-L. 2003, *MNRAS*, 338, 555
- Laurent, O., Mirabel, I. F., Charmandaris, V., et al. 2000, *A&A*, 359, 887
- Levenson, N. A., Radomski, J. T., Packham, C., Mason, R. E., Schaefer, J. J., & Telesco, C. M. 2009, *ApJ*, 703, 390
- Lutz, D., Maiolino, R., Spoon, H. W. W., & Moorwood, A. F. M. 2004, *A&A*, 418, 465
- Malkan, M. A., Gorjian, V., & Tam, R. 1998, *ApJS*, 117, 25
- Malmrose, M. P., Marscher, A. P., Jorstad, S. G., Nikutta, R., & Elitzur, M. 2011, *ApJ*, 732, 116
- Matt, G., Guainazzi, M., Frontera, F., et al. 1997, *A&A*, 325, L13
- Matt, G., Guainazzi, M., Maiolino, R., et al. 1999, *A&A*, 341, L39
- Matt, G., Fabian, A. C., Guainazzi, M., Iwasawa, K., Bassani, L., & Malaguti, G. 2000, *MNRAS*, 318, 173
- Molina, M., et al. 2008, *MNRAS*, 390, 1217
- Moorwood, A. F. M., van der Werf, P. P., Kotilainen, J. K., Marconi, A., & Oliva, E. 1996, *A&A*, 308, L1
- Mor, R., Netzer, H., & Elitzur, M. 2009, *ApJ*, 705, 298

- Moran, E. C., Lehnert, M. D., & Helfand, D. J. 1999, *ApJ*, 526, 649
- Mullaney, J. R., Alexander, D. M., Goulding, A. D., & Hickox, R. C. 2011, *MNRAS*, 414, 1082
- Murakami, H., Baba, H., Barthel, P., et al. 2007, *PASJ*, 59, 369
- Mushotzky, R. F., Winter, L. M., McIntosh, D. H., & Tueller, J. 2008, *ApJ*, 684, L65
- Neškova, M., Sirocky, M. M., Nikutta, R., Ivezić, Ž., & Elitzur, M. 2008, *ApJ*, 685, 160
- Persic, M., & Rephaeli, Y. 2002, *A&A*, 382, 843
- Pietsch, W., et al. 2001, *A&A*, 365, L174
- Pier, E. A., & Krolik, J. H. 1993, *ApJ*, 418, 673
- Plotkin, R. M., Anderson, S. F., Brandt, W. N., et al. 2011, *arXiv:1112.5162*
- Polletta, M., Tajer, M., Maraschi, L., et al. 2007, *ApJ*, 663, 81
- Ranalli, P., Comastri, A., & Setti, G. 2003, *A&A*, 399, 39
- Ranalli, P., Comastri, A., Origlia, L., & Maiolino, R. 2008, *MNRAS*, 386, 1464
- Rigby, J. R., Diamond-Stanic, A. M., & Aniano, G. 2009, *ApJ*, 700, 1878
- Risaliti, G., et al. 2009, *ApJ*, 705, L1
- Russell, H. R., Fabian, A. C., Sanders, J. S., et al. 2010, *MNRAS*, 402, 1561
- Sambruna, R. M., Eracleous, M., & Mushotzky, R. F. 1999, *ApJ*, 526, 60
- Sanders, D. B., & Mirabel, I. F. 1996, *ARA&A*, 34, 749
- Schartmann, M., Meisenheimer, K., Camenzind, M., Wolf, S., Tristram, K. R. W., & Henning, T. 2008, *A&A*, 482, 67
- Schweitzer, M., Lutz, D., Sturm, E., et al. 2006, *ApJ*, 649, 79
- Soria, R., & Motch, C. 2004, *A&A*, 422, 915
- Sturm, E., Lutz, D., Verma, A., et al. 2002, *A&A*, 393, 821
- Sunyaev, R. A., & Titarchuk, L. G. 1980, *A&A*, 86, 121
- Tazaki, F., Ueda, Y., Ishino, Y., Eguchi, S., Isobe, N., Terashima, Y., & Mushotzky, R. F. 2010, *ApJ*, 721, 1340
- Teng, S. H., et al. 2009, *ApJ*, 691, 261
- Tueller, J., Mushotzky, R. F., Barthelmy, S., Cannizzo, J. K., Gehrels, N., Markwardt, C. B., Skinner, G. K., & Winter, L. M. 2008, *ApJ*, 681, 113
- Tueller, J., et al. 2010, *ApJS*, 186, 378
- Unwin, S. C., Wehrle, A. E., Lobanov, A. P., et al. 1997, *ApJ*, 480, 596
- Véron-Cetty, M.-P., & Véron, P. 2010, *A&A*, 518, A10
- Vermeulen, R. C., Ros, E., Kellermann, K. I., et al. 2003, *A&A*, 401, 113
- Vasudevan, R. V., Fabian, A. C., Gandhi, P., Winter, L. M., & Mushotzky, R. F. 2010, *MNRAS*, 402, 1081
- Vignati, P., et al. 1999, *A&A*, 349, L57
- Vignali, C., & Comastri, A. 2002, *A&A*, 381, 834
- Weaver, K. A., Meléndez, M., Mushotzky, R. F., et al. 2010, *ApJ*, 716, 1151
- Winter, L. M., Mushotzky, R. F., Reynolds, C. S., & Tueller, J. 2009, *ApJ*, 690, 1322
- Xu, C., Livio, M., & Baum, S. 1999, *AJ*, 118, 1169
- Yamamura, I., Makiuti, S., Ikeda, N., Fukuda, Y., Oyabu, S., Koga, T., & White, G. J. 2010, *VizieR Online Data Catalogue*, 2298, 0
- Yamauchi, C., Fujishima, S., Ikeda, N., et al. 2011, *PASP*, 123, 852
- Zakamska, N. L., Strauss, M. A., Krolik, J. H., et al. 2003, *AJ*, 126, 2125
- Zezas, A. L., Georgantopoulos, I., & Ward, M. J. 1998, *MNRAS*, 301, 915

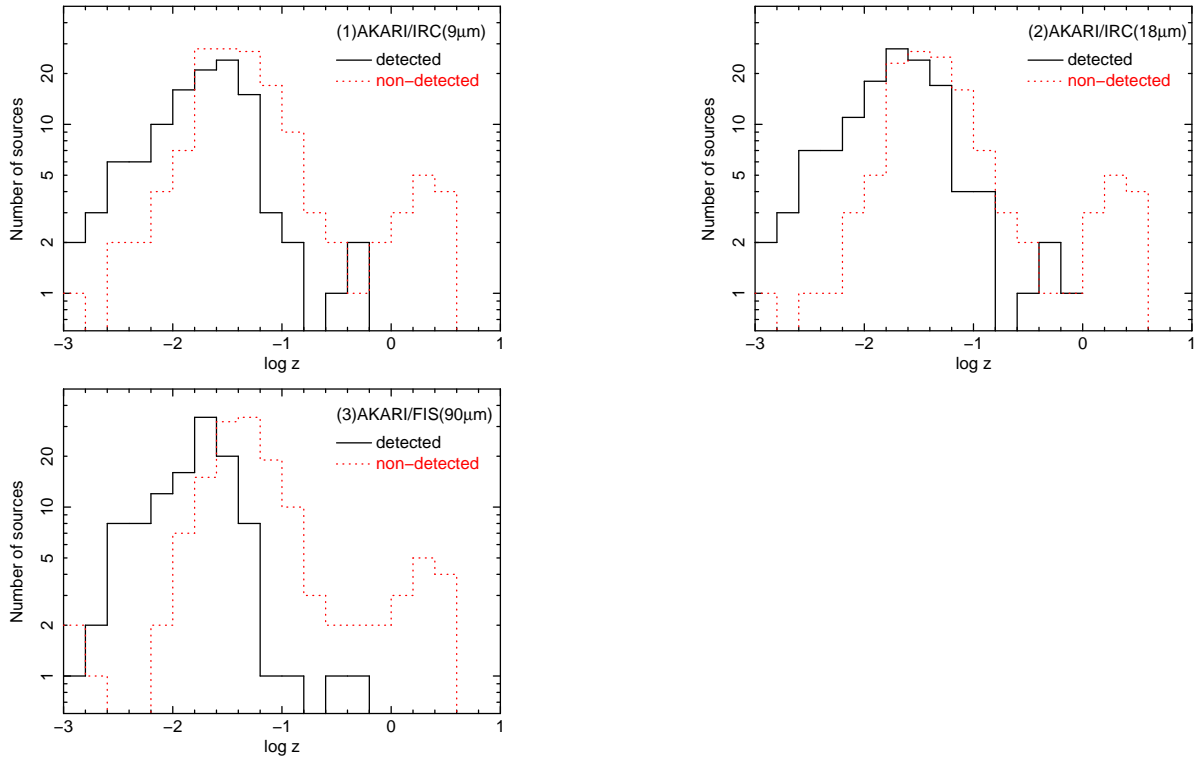


FIG. 1.— Redshift distribution of all AGN detected in the *Swift*/BAT. The values of redshift were taken from those listed in the 22-month *Swift*/BAT hard X-ray survey catalogue (Tueller et al. 2010). The abscissas are logarithmic redshift. The ordinates are total number of sources. Black solid lines show the *AKARI* detected sources (*AKARI*/PSC; *FQUAL* = 3 only), while red dotted lines show the sources not listed in the *AKARI*/PSC.

TABLE 1
 AKARI INFRARED PROPERTIES OF THE AGN IN THE 22-MONTH
Swift/BAT CATALOG

Serial NO.	BAT No.	Object name	Flux ₀₉ (mJy)	Flux ₁₈ (mJy)	Flux ₉₀ (mJy)	log L_X (erg s ⁻¹)	Redshift	Type
(1)	(2)	(3)	(4)	(5)	(6)	(7)	(8)	(9)
1	1	Mrk 335	128 ± 3	223 ± 46	...	43.52 ± 0.07	0.0258	Sy1.2
2	2	Mrk 1501	...	134 ± 21	...	44.82 ± 0.05	0.0893	Sy1.2/RIM
3	3	2MASX J00253292+6821442	75 ± 8	216 ± 22	...	42.94 ± 0.09	0.0120	Sy2
4	8	NGC 235A	...	295 ± 32	...	43.61 ± 0.05	0.0222	Sy1 ^a
5	9	Mrk 348	...	593 ± 43	736 ± 60	43.79 ± 0.04	0.0150	Sy2
6	21	NGC 526A	141 ± 14	292 ± 26	...	43.64 ± 0.04	0.0191	Sy1.5
7	22	Fairall 9	229 ± 20	440 ± 24	...	44.35 ± 0.04	0.0470	Sy1
8	23	NGC 513	2533 ± 107	43.20 ± 0.08	0.0195	Sy2
9	24	NGC 612	135 ± 34	...	2604 ± 261	43.98 ± 0.04	0.0298	Sy2 ^a /RL
10	25	ESO 297-018	672 ± 67	43.97 ± 0.04	0.0252	Sy2
11	27	MCG -01-05-047	...	139 ± 7	2597 ± 225	43.22 ± 0.07	0.0172	Sy2
12	28	NGC 788	...	312 ± 25	...	43.54 ± 0.04	0.0136	Sy2
13	34	NGC 931	349 ± 12	763 ± 48	2430 ± 64	43.56 ± 0.04	0.0167	Sy1.5
14	35	IC 1816	55 ± 32	265 ± 20	1473 ± 54	43.17 ± 0.07	0.0170	Sy1.8
15	36	NGC 973	...	93 ± 77	1704 ± 69	43.21 ± 0.07	0.0162	Sy2
16	37	NGC 985	165 ± 14	368 ± 38	1291 ± 16	44.11 ± 0.05	0.0430	Sy1
17	41	NGC 1052	146 ± 34	377 ± 17	793 ± 36	42.27 ± 0.07	0.0050	Sy2/RL
18	42	NGC 1068	24923 ± 188	72285 ± 27	202591 ± 28886	42.03 ± 0.06	0.0038	Sy2/CT
19	43	[HB89] 0241+622	300 ± 14	635 ± 34	576 ± 80	44.52 ± 0.04	0.0440	Sy1/RIM
20	44	2MASX J02485937+2630391	1398 ± 25	44.42 ± 0.08	0.0579	Sy2
21	47	NGC 1142	265 ± 16	380 ± 71	7036 ± 178	44.23 ± 0.04	0.0289	Sy2
22	50	NGC 1194	169 ± 7	415 ± 56	530 ± 42	43.13 ± 0.07	0.0136	Sy1
23	54	NGC 1275 (3C 084)	442 ± 26	1989 ± 21	6928 ± 245	43.63 ± 0.04	0.0176	Sy2/RL
24	55	B2 0321+33 NED02	...	95 ± 4	...	44.56 ± 0.07	0.0610	Sy1
25	57	PKS 0326-288	...	152 ± 7	...	44.88 ± 0.09	0.1080	Sy1.9
26	60	NGC 1365	2234 ± 38	5364 ± 43	80384 ± 13546	42.64 ± 0.04	0.0055	Sy1.8/CT
27	64	ESO 548-G081	968 ± 61	43.28 ± 0.04	0.0145	Sy1
28	68	2MASX J03534246+3714077	827 ± 78	43.06 ± 0.10	0.0183	Sy2
29	70	ESO 549- G049	156 ± 15	302 ± 43	2976 ± 170	43.56 ± 0.09	0.0263	Sy1 ^a
30	72	IRAS 04124-0803	168 ± 12	423 ± 39	...	43.86 ± 0.08	0.0379	Sy1
31	73	3C 111.0	61 ± 7	44.82 ± 0.04	0.0485	Sy1/RL
32	75	1H 0419-577	...	106 ± 21	...	44.66 ± 0.06	0.1040	Sy1
33	77	3C 120	203 ± 20	497 ± 68	1468 ± 85	44.41 ± 0.04	0.0330	Sy1/RL
34	78	MCG -02-12-050	682 ± 111	43.75 ± 0.08	0.0364	Sy1.2
35	79	UGC 03142	1581 ± 79	43.51 ± 0.07	0.0217	Sy1
36	80	2MASX J04440903+2813003	90 ± 18	...	1427 ± 214	43.25 ± 0.04	0.0113	Sy2
37	83	CGCG 420-015	173 ± 7	471 ± 22	624 ± 32	43.85 ± 0.07	0.0294	Sy2
38	84	ESO 033-G 002	163 ± 7	387 ± 15	646 ± 120	43.23 ± 0.07	0.0181	Sy2
39	85	LEDA 097068	218 ± 13	581 ± 27	852 ± 53	44.36 ± 0.07	0.0577	Sy1
40	87	IRAS 05078+1626	166 ± 14	748 ± 46	957 ± 41	43.78 ± 0.04	0.0179	Sy1.5
41	89	Ark 120	252 ± 18	253 ± 33	...	44.17 ± 0.04	0.0323	Sy1
42	90	ESO 362-18	166 ± 31	366 ± 36	1277 ± 88	43.29 ± 0.04	0.0125	Sy1.5
43	93	PKS 0521-36	97 ± 0.1	216 ± 20	...	44.32 ± 0.06	0.0553	Blazar/BL Lac
44	109	NGC 2110	300 ± 19	566 ± 30	4594 ± 47	43.63 ± 0.04	0.0078	Sy2
45	110	MCG +08-11-011	340 ± 18	1283 ± 35	2377 ± 62	43.91 ± 0.04	0.0205	Sy1.5
46	112	2MASX J05580206-3820043	348 ± 15	536 ± 17	...	43.96 ± 0.04	0.0339	Sy1
47	113	IRAS 05589+2828	201 ± 7	454 ± 33	955 ± 79	44.17 ± 0.05	0.0330	Sy1
48	114	ESO 005-G 004	537 ± 46	520 ± 46	8501 ± 407	42.54 ± 0.05	0.0062	Sy2
49	115	Mrk 3	321 ± 5	1890 ± 49	2939 ± 282	43.76 ± 0.04	0.0135	Sy2
50	118	ESO 490-IG026	1409 ± 41	43.72 ± 0.04	0.0248	Sy1.2
51	121	Mrk 6	180 ± 8	522 ± 23	920 ± 55	43.73 ± 0.04	0.0188	Sy1.5
52	122	UGC 03601	385 ± 23	43.41 ± 0.06	0.0171	Sy1.5
53	125	Mrk 79	276 ± 6	611 ± 38	1358 ± 64	43.68 ± 0.04	0.0222	Sy1.2
54	127	Mrk 10	918 ± 44	43.73 ± 0.07	0.0293	Sy1.2
55	131	2MASX J07595347+2323241	105 ± 22	...	2820 ± 120	43.86 ± 0.07	0.0292	Sy2
56	132	IC 0486	1213 ± 61	43.67 ± 0.09	0.0269	Sy1
57	133	Phoenix Galaxy	274 ± 19	1310 ± 6	1196 ± 62	43.29 ± 0.04	0.0135	Sy2
58	134	FAIRALL 0272	791 ± 58	43.58 ± 0.07	0.0218	Sy2
59	138	FAIRALL 1146	157 ± 14	441 ± 30	1059 ± 152	43.82 ± 0.06	0.0316	Sy1.5
60	145	IRAS 09149-6206	407 ± 7	792 ± 17	1735 ± 48	44.33 ± 0.06	0.0573	Sy1
61	146	Mrk 704	256 ± 30	469 ± 20	...	43.79 ± 0.06	0.0292	Sy1.5
62	148	MCG -01-24-012	...	263 ± 44	...	43.55 ± 0.06	0.0196	Sy2
63	149	MCG +04-22-042	78 ± 15	178 ± 47	...	43.97 ± 0.05	0.0323	Sy1.2
64	152	Mrk 705	99 ± 21	213 ± 44	926 ± 84	43.56 ± 0.08	0.0291	Sy1.2
65	153	NGC 2992	299 ± 49	827 ± 54	9220 ± 194	42.76 ± 0.05	0.0077	Sy2

TABLE 1
Continued.

Serial No.	BAT No.	Object name	Flux ₀₉ (mJy)	Flux ₁₈ (mJy)	Flux ₉₀ (mJy)	log L_X (erg s ⁻¹)	Redshift	Type
(1)	(2)	(3)	(4)	(5)	(6)	(7)	(8)	(9)
66	154	MCG -05-23-016	384 ± 14	1391 ± 21	1277 ± 84	43.48 ± 0.04	0.0085	Sy2
67	158	NGC 3081	167 ± 13	699 ± 41	2364 ± 131	43.12 ± 0.04	0.0080	Sy2
68	159	NGC 3079	...	1561 ± 83	59311 ± 1906	41.97 ± 0.05	0.0037	Sy2/CT
69	163	ESO 374-G 044	...	307 ± 74	...	43.66 ± 0.08	0.0284	Sy2
70	164	NGC 3227	444 ± 71	1128 ± 44	10596 ± 535	42.63 ± 0.04	0.0039	Sy1.5
71	165	NGC 3281	415 ± 9	1509 ± 29	6011 ± 458	43.31 ± 0.04	0.0107	Sy2/CT
72	167	LEDA 093974	96 ± 23	256 ± 68	941 ± 26	43.62 ± 0.07	0.0239	Sy2
73	171	NGC 3516	262 ± 20	651 ± 16	1317 ± 83	43.29 ± 0.04	0.0088	Sy1.5
74	179	NGC 3783	502 ± 10	1530 ± 41	2716 ± 108	43.56 ± 0.04	0.0097	Sy1
75	185	NGC 3998	98 ± 22	133 ± 20	451 ± 16	41.87 ± 0.06	0.0035	LINER ^a
76	187	LEDA 38038	166 ± 8	614 ± 41	1631 ± 123	43.83 ± 0.06	0.0280	Sy2
77	188	NGC 4051	346 ± 30	885 ± 42	4557 ± 254	41.66 ± 0.04	0.0023	Sy1.5
78	189	ARK 347	...	102 ± 56	...	43.59 ± 0.06	0.0224	Sy2
79	190	NGC 4102	1082 ± 49	3287 ± 74	54050 ± 2235	41.61 ± 0.06	0.0028	LINER/CT
80	191	Mrk 198	584 ± 97	43.40 ± 0.08	0.0242	Sy2
81	192	NGC 4138	2161 ± 74	41.82 ± 0.05	0.0030	Sy1.9
82	193	NGC 4151	1032 ± 19	3629 ± 72	4594 ± 126	43.13 ± 0.04	0.0033	Sy1.5
83	195	NGC 4235	401 ± 50	42.49 ± 0.09	0.0080	Sy1
84	196	Mrk 766	220 ± 13	859 ± 20	3312 ± 190	42.91 ± 0.05	0.0129	Sy1.5
85	197	M 106	387 ± 47	449 ± 72	...	41.10 ± 0.09	0.0015	LINER
86	200	NGC 4388	462 ± 21	1589 ± 31	10349 ± 637	43.69 ± 0.04	0.0084	Sy2
87	204	3C 273	276 ± 3	454 ± 7	814 ± 56	46.28 ± 0.04	0.1583	Blazar/FSRQ
88	206	NGC 4507	510 ± 4	1163 ± 31	4370 ± 117	43.80 ± 0.04	0.0118	Sy2
89	207	ESO 506-G027	114 ± 19	207 ± 1	613 ± 73	44.24 ± 0.04	0.0250	Sy2
90	209	NGC 4593	...	569 ± 5	...	43.20 ± 0.04	0.0090	Sy1
91	211	WKK 1263	...	170 ± 24	769 ± 29	43.68 ± 0.08	0.0244	Sy2 ^a
92	215	3C 279	265 ± 57	626 ± 2	2024 ± 117	46.46 ± 0.06	0.5362	Blazar/FSRQ
93	221	NGC 4945	8811 ± 325	9945 ± 495	...	42.38 ± 0.04	0.0019	LINER ^b /CT
94	222	ESO 323-077	472 ± 3	902 ± 17	6945 ± 236	43.33 ± 0.06	0.0150	Sy1.2
95	223	NGC 4992	59 ± 10	...	352 ± 42	43.89 ± 0.04	0.0251	Sy2 ^c
96	225	MCG -03-34-064	453 ± 11	1873 ± 45	4634 ± 106	43.23 ± 0.06	0.0165	Sy1.8
97	226	Cen A	10191 ± 2305	13148 ± 1049	102187 ± 12824	42.78 ± 0.04	0.0018	Sy2/RL
98	228	MCG -06-30-015	280 ± 32	591 ± 11	1035 ± 119	42.97 ± 0.04	0.0077	Sy1.2
99	229	NGC 5252	415 ± 120	43.94 ± 0.04	0.0230	Sy1.9
100	230	4U 1344-60	207 ± 9	556 ± 28	...	43.50 ± 0.04	0.0129	Sy1.5
101	231	IC 4329A	769 ± 12	1790 ± 34	1785 ± 210	44.23 ± 0.04	0.0160	Sy1.2
102	233	Mrk 279	141 ± 9	388 ± 28	...	43.99 ± 0.04	0.0304	Sy1.5
103	235	Circinus Galaxy	13910 ± 173	41447 ± 265	253567 ± 64752	42.03 ± 0.04	0.0014	Sy2 ^d /CT
104	236	NGC 5506	823 ± 27	2240 ± 69	8413 ± 302	43.29 ± 0.04	0.0062	Sy1.9
105	237	NGC 5548	157 ± 5	409 ± 40	1073 ± 237	43.68 ± 0.04	0.0172	Sy1.5
106	238	ESO 511-G030	847 ± 150	43.67 ± 0.06	0.0224	Sy1
107	239	SBS 1419+480	46 ± 6	189 ± 13	...	44.34 ± 0.07	0.0723	Sy1.5
108	241	Mrk 817	188 ± 10	669 ± 27	1575 ± 60	43.64 ± 0.07	0.0314	Sy1.5
109	242	NGC 5728	176 ± 21	418 ± 31	11383 ± 420	43.26 ± 0.04	0.0093	Sy2/CT
110	246	WKK 4438	94 ± 15	266 ± 12	1105 ± 86	43.01 ± 0.10	0.0160	Sy1
111	247	IC 4518A	243 ± 27	677 ± 22	7039 ± 243	43.24 ± 0.06	0.0163	Sy2
112	248	Mrk 841	126 ± 13	372 ± 25	...	43.89 ± 0.07	0.0364	Sy1
113	254	NGC 5899	4683 ± 184	42.50 ± 0.08	0.0086	Sy2
114	257	MCG -01-40-001	2304 ± 108	43.59 ± 0.06	0.0227	Sy2
115	258	Mrk 290	...	151 ± 13	...	43.65 ± 0.06	0.0296	Sy1
116	264	NGC 5995	325 ± 19	671 ± 4	4580 ± 329	43.76 ± 0.06	0.0252	Sy2
117	277	Mrk 1498	67 ± 12	214 ± 21	...	44.42 ± 0.04	0.0547	Sy1.9
118	285	3C 345	102 ± 7	353 ± 8	...	46.37 ± 0.08	0.5928	Blazar/FSRQ
119	292	NGC 6240	350 ± 15	1489 ± 12	23179 ± 433	43.94 ± 0.04	0.0245	Sy2/CT
120	295	1RXS J165605.6-520345	135 ± 13	248 ± 24	1109 ± 84	44.35 ± 0.08	0.0540	Sy1.2
121	317	NGC 6300	277 ± 24	1336 ± 97	14928 ± 1066	42.45 ± 0.04	0.0037	Sy2
122	360	[HB89] 1821+643	131 ± 4	326 ± 10	635 ± 34	45.49 ± 0.08	0.2970	Sy1/RIM
123	370	3C 382	120 ± 12	44.75 ± 0.04	0.0579	Sy1/RL
124	372	FAIRALL 0049	411 ± 20	920 ± 59	2619 ± 180	43.38 ± 0.07	0.0202	Sy2
125	374	ESO 103-035	300 ± 25	1446 ± 12	1227 ± 77	43.60 ± 0.04	0.0133	Sy2
126	377	3C 390.3	90 ± 10	242 ± 17	...	44.84 ± 0.04	0.0561	Sy1/RL
127	378	Fairall 0051	301 ± 7	697 ± 62	1705 ± 180	43.27 ± 0.06	0.0142	Sy1
128	401	ESO 141-G 055	150 ± 5	233 ± 38	...	44.14 ± 0.05	0.0360	Sy1
129	404	2MASX J19301380+3410495	130 ± 12	254 ± 23	...	44.41 ± 0.06	0.0629	Sy1
130	405	2MASS J19334715+3254259	101 ± 10	269 ± 8	...	44.19 ± 0.08	0.0578	Sy1.2

TABLE 1
Continued.

Serial No.	BAT No.	Object name	Flux ₀₉ (mJy)	Flux ₁₈ (mJy)	Flux ₉₀ (mJy)	log L_X (erg s ⁻¹)	Redshift	Type
(1)	(2)	(3)	(4)	(5)	(6)	(7)	(8)	(9)
131	407	NGC 6814	...	258 ± 29	6954 ± 350	42.63 ± 0.04	0.0052	Sy1.5
132	415	Cygnus A (3C 405)	...	418 ± 17	2455 ± 78	44.89 ± 0.04	0.0561	Sy2/RL
133	418	NGC 6860	155 ± 13	357 ± 61	1369 ± 73	43.46 ± 0.05	0.0149	Sy1
134	420	MCG +04-48-002	388 ± 11	538 ± 16	12160 ± 289	43.53 ± 0.04	0.0139	Sy2
135	425	4C +74.26	147 ± 6	175 ± 9	...	45.04 ± 0.04	0.1040	Sy1/RL
136	426	RX J2044.0+2833	...	199 ± 46	...	44.10 ± 0.07	0.0500	Sy1
137	427	Mrk 509	247 ± 18	499 ± 17	...	44.35 ± 0.04	0.0344	Sy1.2
138	428	IC 5063	...	2246 ± 26	3821 ± 141	43.35 ± 0.04	0.0114	Sy2
139	429	2MASX J21140128+8204483	71 ± 5	105 ± 32	...	44.77 ± 0.05	0.0840	Sy1/RL
140	434	4C 50.55	...	188 ± 21	...	44.15 ± 0.04	0.0200	Sy1 ^a /RL
141	435	SWIFT J212745.58+565635.6	211 ± 15	435 ± 17	...	43.22 ± 0.04	0.0147	Sy1
142	441	1RXS J213623.1-622400	...	142 ± 11	...	44.43 ± 0.06	0.0588	Sy1
143	445	Mrk 520	146 ± 12	320 ± 11	5040 ± 100	43.70 ± 0.07	0.0266	Sy1.9
144	446	NGC 7172	316 ± 17	424 ± 44	8087 ± 218	43.44 ± 0.04	0.0087	Sy2
145	447	BL Lac	247 ± 36	319 ± 34	937 ± 122	44.62 ± 0.05	0.0686	Blazar/BL Lac
146	449	NGC 7213	360 ± 35	...	2943 ± 146	42.59 ± 0.05	0.0058	Sy1.5
147	451	3C 445	141 ± 13	358 ± 6	...	44.44 ± 0.05	0.0562	Sy1.5/RL
148	452	MCG +02-57-002	575 ± 39	43.54 ± 0.09	0.0290	Sy1.5
149	455	NGC 7314	...	304 ± 58	4499 ± 258	42.33 ± 0.05	0.0048	Sy1.9
150	456	NGC 7319	88 ± 14	158 ± 8	576 ± 39	43.60 ± 0.05	0.0225	Sy2
151	457	Mrk 915	...	482 ± 284	...	43.76 ± 0.06	0.0241	Sy1
152	460	3C 454.3	...	498 ± 6	...	47.37 ± 0.04	0.8590	Blazar/FSRQ
153	463	UGC 12282	1284 ± 124	43.16 ± 0.08	0.0170	Sy1.9
154	465	NGC 7469	767 ± 17	2692 ± 60	27694 ± 1738	43.55 ± 0.05	0.0163	Sy1.2
155	466	Mrk 926	60 ± 3	214 ± 36	647 ± 119	44.65 ± 0.04	0.0469	Sy1.5
156	467	NGC 7582	1368 ± 90	3287 ± 199	60906 ± 6037	42.63 ± 0.04	0.0052	Sy2
157	468	NGC 7603	295 ± 11	321 ± 12	1340 ± 104	43.91 ± 0.04	0.0295	Sy1.5
158	473	LCRS B232242.2-384320	654 ± 80	43.79 ± 0.08	0.0359	Sy1

NOTE. — Col. (1): serial number. Col. (2): Object number in the 22-month *Swift*/BAT hard X-ray survey catalog (Tueller et al. 2010). Col. (3): Object name. Col. (4)(5)(6): The flux and error in 9, 18, and 90 μm taken from *AKARI*/PSC in units of mJy. Col. (7): The logarithmic luminosity and error in hard X-ray band (14-195 keV) taken from Tueller et al. (2010), in units of erg s⁻¹. Col. (8): Redshift. Col. (9): Optical AGN type taken from Tueller et al. (2010) or from other literature sources as follows:

REFERENCES. — ^aVéron-Cetty & Véron (2010); ^bMoorwood et al. (1996); ^cBodaghee et al. (2007); ^dMatt et al. (2000)

TABLE 2
SUMMARY OF CROSS-IDENTIFICATIONS

<i>AKARI</i> detector		Source type				Total	Excluded source
		Sy1	Sy2	LINER	Blazar		
(1)	(2)	(3)	(4)	(5)	(6)	(7)	(8)
IRC 9 (μm)	detection	59	43	4	5	111	2
	non-detection	66	56	2	21	145	10
IRC 18 (μm)	detection	67	52	4	6	129	5
	non-detection	57	47	2	20	126	8
FIS 90 (μm)	detection	48	60	2	3	113	3
	non-detection	76	41	4	22	143	9

NOTE. — Col.(1): The *AKARI* instruments and the center bands. Col.(3): The number of source detection and non-detection of Seyfert 1 type AGN including Seyfert 1.2 and 1.5. Col.(4): The number of source detection and non-detection of Seyfert 2 type AGN including Seyfert 1.8 and 1.9. Col.(5): The number of source detection and non-detection of LINERs. Col.(6): The number of source detection and non-detection of Blazars. Col.(7): The total number of source detection and non-detection, i.e., sum of columns (3) through (6). Col.(8): The number of excluded sources, which are confused or confusing sources as defined by Tueller et al. (2010).

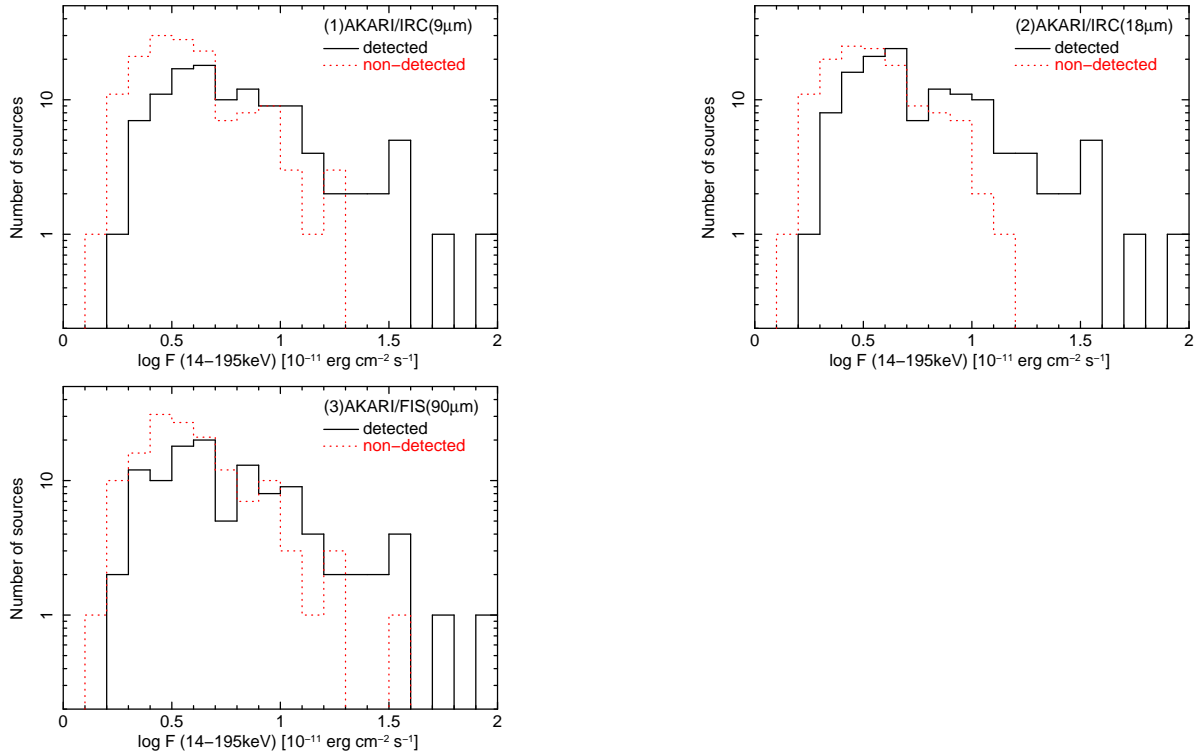


FIG. 2.— Hard X-ray flux distributions for the *Swift*/BAT sources. The abscissa is logarithmic hard X-ray flux. The ordinate is the number of sources. Black solid lines show the *AKARI* detected sources, while red dotted lines show those are not detected by *AKARI* in 3σ .

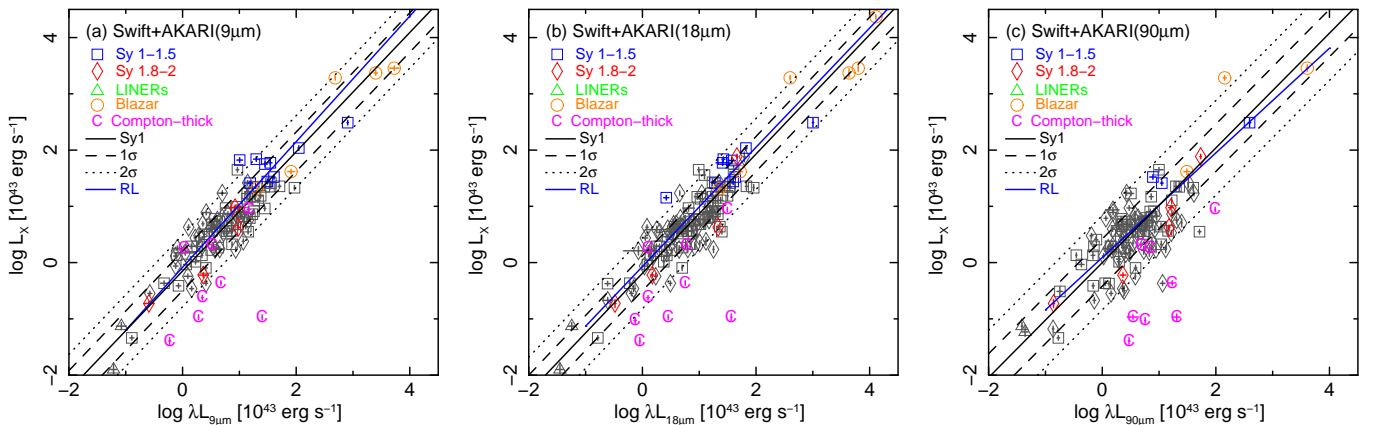


FIG. 3.— Logarithmic luminosity correlations between the *AKARI* and *Swift*/BAT. The ordinates are hard X-ray (14–195 keV) luminosities, and the abscissas are IR luminosities at (a) $9\ \mu\text{m}$, (b) $18\ \mu\text{m}$, and (c) $90\ \mu\text{m}$. Symbols indicates the AGN types (Seyfert 1, Seyfert 2, LINERs, and Blazars). Color symbols in the plots are radio-loud AGN and blazars. Gray symbols are radio-quiet AGN. Magenta character “C” indicates Compton thick sources. The black and blue solid lines are the correlation fitted to only Seyfert 1s (“Sy1”) and “RL”, by using the liner regression algorithm, respectively. The dashed and dotted lines show the standard deviation of the correlation; 1σ and 2σ .

TABLE 3
SUMMARY OF THE FITTING RESULTS

<i>AKARI</i> detector (1)	Subsample (2)	N (3)	ρ (4)	$\rho_{.z}$ (5)	a (6)	b (7)	\bar{r} (8)	σ_r (9)
IRC 9 (μm)	All	111	0.85	0.79	0.22 ± 0.05	0.88 ± 0.04	0.14	0.42
	All, ex CT	103	0.88	0.87	0.13 ± 0.04	0.94 ± 0.04	0.08	0.32
	Sy1	59	0.87	0.85	0.15 ± 0.05	0.94 ± 0.06	0.09	0.30
	Sy1, ex RL	50	0.87	0.69	0.15 ± 0.05	0.99 ± 0.07	0.14	0.26
	Sy2	43	0.58	0.06	0.23 ± 0.08	0.84 ± 0.07	0.17	0.53
	Sy2, ex CT	37	0.70	0.44	0.11 ± 0.07	0.91 ± 0.08	0.06	0.35
	CT	8	0.31	-0.14	0.81 ± 0.28	0.81 ± 0.24	0.87	0.81
	RL	13	0.81	0.89	0.09 ± 0.15	0.90 ± 0.11	-0.14	0.39
	Blazar	5	1.00	0.87	0.11 ± 0.23	0.96 ± 0.10	-0.002	0.36
RL + Blazar	18	0.86	0.88	0.05 ± 0.14	0.95 ± 0.07	-0.03	0.37	
IRC 18 (μm)	All	129	0.84	0.77	0.27 ± 0.05	0.89 ± 0.04	0.19	0.43
	All, exc CT	120	0.86	0.84	0.18 ± 0.04	0.94 ± 0.03	0.14	0.34
	Sy1	67	0.84	0.75	0.18 ± 0.06	0.94 ± 0.06	0.13	0.31
	Sy1, ex RL	58	0.84	0.68	0.20 ± 0.06	0.97 ± 0.07	0.17	0.28
	Sy2	52	0.62	0.31	0.31 ± 0.07	0.86 ± 0.06	0.27	0.53
	Sy2, ex CT	45	0.72	0.57	0.18 ± 0.06	0.94 ± 0.06	0.17	0.38
	CT	9	0.55	-0.12	0.93 ± 0.26	0.86 ± 0.15	1.00	0.81
	RL	13	0.90	0.80	0.07 ± 0.18	0.94 ± 0.11	-0.02	0.41
	Blazar	6	1.00	0.75	0.04 ± 0.16	0.98 ± 0.07	-0.03	0.38
RL + Blazar	19	0.93	0.84	0.04 ± 0.15	0.97 ± 0.07	-0.02	0.39	
FIS 90 (μm)	All	113	0.57	0.48	0.21 ± 0.06	0.88 ± 0.06	0.15	0.58
	All, ex CT	106	0.65	0.64	0.10 ± 0.05	0.94 ± 0.06	-0.08	0.48
	Sy1	48	0.77	0.66	0.002 ± 0.074	0.98 ± 0.08	-0.01	0.39
	Sy1, ex RL	45	0.75	0.37	0.007 ± 0.079	1.01 ± 0.11	0.01	0.39
	Sy2	60	0.33	0.06	0.32 ± 0.08	0.91 ± 0.06	0.29	0.63
	Sy2, ex CT	53	0.46	0.25	0.17 ± 0.07	0.94 ± 0.07	0.18	0.53
	CT	8	0.50	-0.26	1.24 ± 0.16	0.65 ± 0.05	1.32	0.69
	RL	8	0.79	0.83	0.09 ± 0.18	0.93 ± 0.09	0.02	0.42
	Blazar	3	1.00	1.00	-	-	-0.37	0.67
RL + Blazar	11	0.91	0.81	0.08 ± 0.18	0.89 ± 0.11	-0.08	0.50	

NOTE. — Col.(1): The *AKARI* data used for the correlation studies. Col.(2): Subsamples used for fitting (See Sec. 3.2). Col. (3): number of sources in each subsample. Col. (4): Spearman's Rank correlation coefficient (ρ). Col. (5): partial correlation coefficient ($\rho_{.z}$) estimated excluding the effect of the redshift. Col. (6): regression slope and its $1\text{-}\sigma$ uncertainty computed with the algorithm of OLS bisector for Equation (1). Col. (7): same as column (6) but for regression intercept and its $1\text{-}\sigma$ uncertainty. Col. (8) (9): average and standard deviation of the luminosity ratio $r = \log(L_{\text{IR}}/L_X)$.

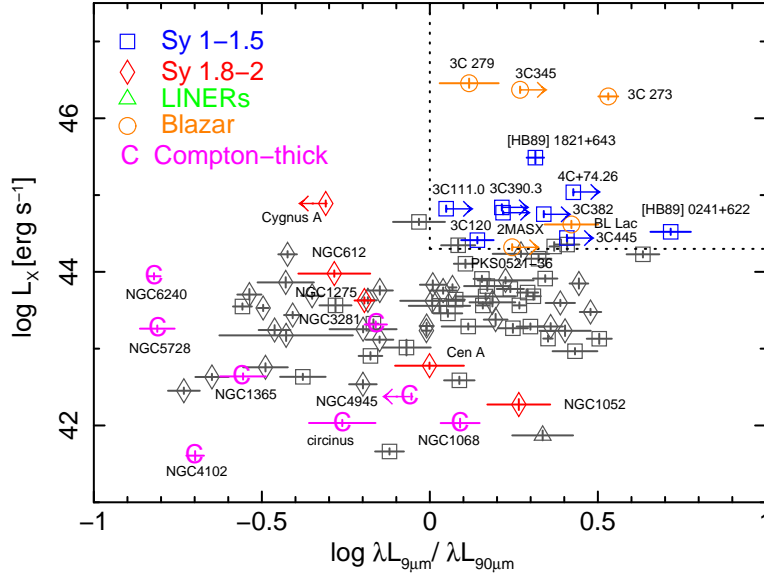


FIG. 4.— Absolute magnitude ($\log L_X$) vs. Color ($\log \lambda L_{9\mu\text{m}}/\lambda L_{90\mu\text{m}}$) diagram for 89 *Swift*/BAT and *AKARI* detected sources. Color symbols in the plots are radio-loud AGN and blazars. Gray symbols are radio-quiet AGN. Magenta character “C” indicates Compton thick sources. The radio loud sources are located in the upper-right region as indicated by the dotted box. NGC3079, one of the Compton-thick sources, is out of the figure range, ($\log L_X, \log \lambda L_{9\mu\text{m}}/\lambda L_{90\mu\text{m}}$) = (41.93, -1.69).

TABLE 4
PROPERTIES OF COMPTON-THICK AGN

No.	Object Name	Type	N_{H} (10^{24} cm^{-2})	Observation
(1)	(2)	(3)	(4)	(5)
42	NGC 1068	Sy2	≥ 10	<i>BeppoSAX</i> ^a
60	NGC 1365	Sy1.8	4.0	<i>Suzaku</i> ^b
159	NGC 3079	Sy2	10	<i>BeppoSAX</i> ^c
165	NGC 3281	Sy2	2.0	<i>BeppoSAX</i> ^d
190	NGC 4102	LINER	2.0	<i>Swift</i> /BAT ^e
221	NGC 4945	LINER	5.3	<i>Suzaku</i> ^f
235	Circinus Galaxy	Sy2	4.3	<i>BeppoSAX</i> ^g
242	NGC 5728	Sy2	1.4	<i>Suzaku</i> ^h
292	NGC 6240	Sy2	2.2	<i>BeppoSAX</i> ⁱ

NOTE. — Col.(1): Object number listed in the 22-month *Swift*/BAT hard X-ray survey catalogue (Tueller et al. 2010). Col.(2): Object name. Col.(3): AGN type taken from Tueller et al. (2010). Col.(4): Column density in units of 10^{24} cm^{-2} . Col.(5): The observation of the sources which referred following literatures.

REFERENCES. — ^aMatt et al. (1997); ^bRisaliti et al. (2009); ^cIyamoto et al. (2001); ^dVignali & Comastri (2002); ^eGonzález-Martín et al. (2011); ^fItoh et al. (2008); ^gMatt et al. (1999); ^hComastri et al. (2010); ⁱVignati et al. (1999)

TABLE 5
THE SAMPLE OF STARBURST GALAXIES

Object name	$F_{9\mu\text{m}}$ (Jy)	$F_{90\mu\text{m}}$ (Jy)	$F_{2-10\text{keV}}$ ($10^{-13} \text{ erg cm}^{-2} \text{ s}^{-1}$)	$F_{14-195\text{keV}}$ ($10^{-13} \text{ erg cm}^{-2} \text{ s}^{-1}$)	D (Mpc)
(1)	(2)	(3)	(4)	(5)	(6)
M82	$70.0 \pm 7.00^{\text{a}}$	$2040 \pm 410^{\text{a}}$...	$54.0 \pm 32.0^{\text{b}}$	3.50^{a}
NGC 253	22.6 ± 1.45	$1200 \pm 240^{\text{c}}$	12.3^{d}	$15.7 \text{ (power-law)} \pm 1.57$ $1.76 \text{ (APEC)} \pm 0.18$	2.58^{d}
Arp 220	0.25 ± 0.01	91 ± 63	0.98^{e}	$1.25 \text{ (power-law)} \pm 0.13$ $0.13 \text{ (APEC)} \pm 0.01$	72.9^{e}
NGC 2146	5.52 ± 0.01	168 ± 15	11.4^{f}	$14.7 \text{ (power-law)} \pm 1.47$ $1.65 \text{ (APEC)} \pm 0.17$	16.5^{j}
NGC 3256	2.39 ± 0.01	108 ± 8	5.86^{g}	$7.59 \text{ (power-law)} \pm 0.76$ $0.85 \text{ (APEC)} \pm 0.09$	35.4^{j}
NGC 3310	1.08 ± 0.02	35 ± 1	21.2^{h}	$27.2 \text{ (power-law)} \pm 2.72$ $3.05 \text{ (APEC)} \pm 0.31$	19.8^{j}
NGC 7714	0.29 ± 0.01	11 ± 1	1.58^{i}	$2.03 \text{ (power-law)} \pm 0.20$ $0.23 \text{ (APEC)} \pm 0.02$	38.2^{j}

NOTE. — Col.(1): Object name. Col.(2)(3): Flux and error in 9 and 90 μm in units of Jy, taken from *AKARI*/PSC and the references below. Col.(4): Flux in 2-10 keV band in units of $10^{-13} \text{ erg sec}^{-1} \text{ cm}^{-2}$, taken from the references below. Col.(5): Flux and error in 14-195 keV band in units of $10^{-13} \text{ erg sec}^{-1} \text{ cm}^{-2}$. Except for M82, we simulated the value by using two models, power-law ($\Gamma=2.1$) and APEC (7 keV). Col(6): Distance in Mpc.

REFERENCES. — ^aKaneda et al. (2010); ^bCusumano et al. (2010); ^cKaneda et al. (2009); ^dBauer et al. (2008); ^eTeng et al. (2009); ^fdella Ceca et al. (1999); ^gMoran et al. (1999); ^hZezas et al. (1998); ⁱSoria & Motch (2004); ^jBrandl et al. (2006)

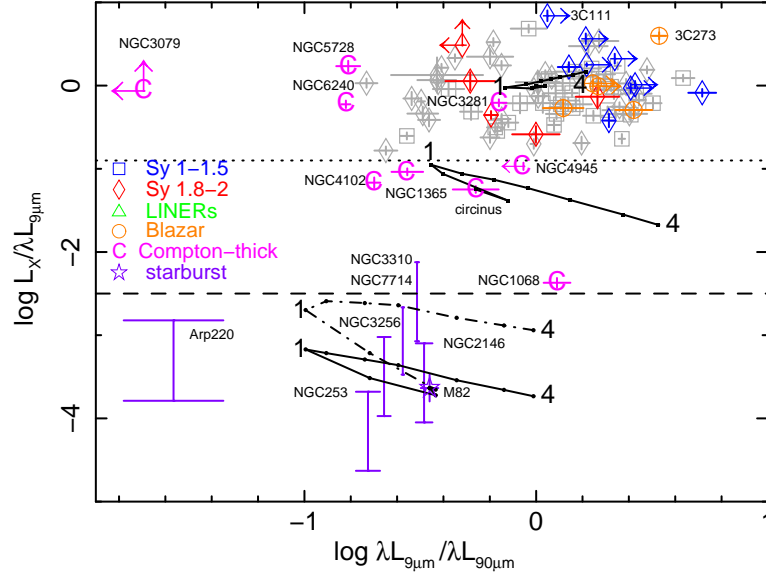


FIG. 5.— Color-color plot of $\log L_X/\lambda L_{9\mu\text{m}}$ vs. $\log \lambda L_{9\mu\text{m}}/\lambda L_{90\mu\text{m}}$ for 89 AGN including 9 Compton-thick (CT) sources and 7 starburst galaxies detected by *AKARI*. Color symbols in the plots are radio-loud AGN and blazars. Gray symbols are radio-quiet AGN. Magenta character “C” indicates Compton thick sources. Open purple stars show starburst galaxies in Table 5, and indicate the estimated hard X-ray (14–195 keV) flux ranges by using the non-thermal (higher bar) and thermal model (lower bar). The dotted line at $\log L_X/\lambda L_{9\mu\text{m}} \sim -0.9$ shows an approximate boundary between normal AGN and CT sources. The dashed line at $\log L_X/\lambda L_{9\mu\text{m}} \sim -2.5$ shows the boundary below which only starburst galaxies are present. The solid lines show how the sources move on the color-color plots when the redshift is changed from 0.0 to 4.0. The lines are calculated for three types of galaxies, a Seyfert galaxy located at (0, 0), Circinus galaxy as a CT AGN, and M82 as a starburst galaxy. The solid and dot-dashed lines for M82 correspond to the different model (non-thermal and thermal, respectively).